Mitochondrial SIRT3 confers neuroprotection in Huntington's disease by regulation of oxidative challenges and mitochondrial dynamics

Luana Naia[1,5], Catarina Carmo[1], Susanna Campesan[2], Lígia Fão[1,3,4], Victoria E. Cotton[2], Jorge Valero[1], Carla Lopes[1,3], Tatiana R. Rosenstock[1], Flaviano Giorgini[2], A. Cristina Rego[1,3,4]*

[1]CNC – Center for Neuroscience and Cell Biology, University of Coimbra, Coimbra, Portugal.
[2]Department of Genetics and Genome Biology, University of Leicester, Leicester, United Kingdom.
[3]CIBB – Center for Innovative Biomedicine and Biotechnology, University of Coimbra, Coimbra, Portugal
[4]Institute of Biochemistry, Faculty of Medicine, University of Coimbra, Coimbra, Portugal.
[5]*Current address:* Karolinska Institutet, Department of Neurobiology, Care Science and Society, Stockholm, Sweden.

*Corresponding author:
Ana Cristina Rego (PhD), Center for Neuroscience and Cell Biology, and Faculty of Medicine, University of Coimbra – polo 1, Rua Larga, 3004-504 Coimbra, Portugal;
acrego@cnc.uc.pt; arego@fmed.uc.pt

Running title: SIRT3 is neuroprotective in Huntington's disease

Keywords: SIRT3, Huntington disease, oxidative stress, mitochondrial function, mitochondrial dynamics

Conflict of interest statement
The authors declare no competing financial interests.

Abstract

SIRT3 is a major regulator of mitochondrial acetylome. Here we show that SIRT3 is neuroprotective in Huntington's disease (HD), a motor neurodegenerative disorder caused by an abnormal expansion of polyglutamines in the huntingtin protein (HTT). Protein and enzymatic analysis revealed that increased SIRT3 is a signature in several HD models, including human HD brain, which is regulated by oxidative species. While loss of SIRT3 further aggravated the oxidative phenotype, antioxidant treatment regularized SIRT3 levels. SIRT3 overexpression promoted the antioxidant effect in cells expressing mutant HTT, leading to enhanced mitochondrial function and balanced dynamics. Decreased Fis1 and Drp1 accumulation in mitochondria induced by SIRT3 expression favored mitochondrial elongation, while the SIRT3 activator ε-viniferin improved anterograde mitochondrial neurite transport, sustaining cell survival. Notably, SIRT3 fly-ortholog dSirt2 overexpression in HD flies ameliorated neurodegeneration and extended lifespan. These findings provide a link between oxidative stress and mitochondrial dysfunction hypotheses in HD and offer an opportunity for therapeutic development.

Introduction

Sirtuin 3 (SIRT3) belongs to a larger family of NAD^+-dependent lysine deacetylases (KDACs) with important roles in metabolism in a variety of organisms. SIRT3 is the major KDAC in mitochondria, controlling more than 1,500 acetylation sites in mitochondrial enzymes involved in fatty acid oxidation, ATP production, pyruvate metabolism and antioxidant defenses [1,2]. SIRT3 is mainly located in the mitochondrial matrix and inner membrane (IMM), but has also been found in the nucleus [3,4] although its functional relevance in this compartment is not clear. In fact, observations demonstrate that unprocessed form of SIRT3 is enzymatically inactive and becomes fully activated upon import to mitochondria followed by cleavage by mitochondrial matrix processing peptidase (MPP) [5]. The mechanisms regulating SIRT3 are multi-faceted. During aging SIRT3 is downregulated, whereas its upregulation reverses aging-associated functional deficits by improving antioxidant activity of the mitochondrial enzyme superoxide dismutase 2 (SOD2) [6]. On the other hand, SIRT3 is upregulated in response to calorie restriction and fasting [7] or to pharmacological inhibition of the mitochondrial electron transport chain [8], highlighting its critical role in stress, adaptive responses and control of lifespan. In accordance, the Haigis lab has shown that under normal physiological conditions a pool of SIRT3 is sequestered at the MIM, whereas under mitochondrial stress such as matrix pH reduction, SIRT3 redistributes to other binding substrates potentiating their rapid deacetylation [9]. This elegant study provided clear evidence that the binding profile of SIRT3 dynamically changes according to mitochondrial environment.

Despite being the most abundant sirtuin in the brain [10], the neuronal role of SIRT3 has only recently been deeply explored [11]. Initial studies indicated that SIRT3 is neuroprotective by enhancing mitochondrial antioxidant capacity and biogenesis through the Peroxisome Proliferator-Activated Receptor Gamma (PGC-1α)/Estrogen-related receptor alpha (ERRα)-SIRT3 pathway [12]. In neurodegeneration models, as in the case of Alzheimer's disease *App*$^{NL-G-F}$ knock-in mice, SIRT3 was described to be critical for GABAergic synaptic homeostasis, improving behavior and neuronal adaptations to intermediate fasting [13].

Improvements in neuronal activity have been linked to the ability of SIRT3 to deacetylate mitochondrial p53, leading to increased mitochondrial DNA transcription [14]. The absence of SIRT3 has also been found to enhance striatal neuron toxicity in mice where mitochondrial complex II was irreversibly inhibited using 3-nitropropionic acid (3-NP) [11]. Indeed, systemic administration of 3-NP produces preferential degeneration in the caudate–putamen that resembles many behavioral and anatomical features of Huntington's disease (HD) [15]. HD is a fatal genetic neurodegenerative disorder that gradually impairs memory, cognitive skills and normal movements of the affected individuals and for which no disease modifying treatments exist. Our group has previously shown that pharmacological activation of SIRT1 by resveratrol ameliorates mitochondrial dysfunction and delays HD-related motor symptoms by modifying the expression of mitochondrial-encoded complex subunits [16]. Another study found that the semisynthetic resveratrol derivative trans-ε-viniferin mediates SIRT3-dependent AMP-activated protein kinase (AMPK) activation, replenishing cellular NAD^+ levels and cell survival in HD striatal cells [17].

Despite encouraging data that pharmacological activation of sirtuins prevents energy depletion that contributes to neurodegeneration, untangling the off-target effects of these polyphenols is a current challenge. Remarkably, no studies exist which explore the effects of directly targeting SIRT3 in HD. In the present study, we provide evidence that human caudate obtained from HD patients as well as neuronal and peripheral models expressing the mutant form of the *HD* gene display a stress-related increase in SIRT3 activity, which can be reverted upon antioxidant treatment. Under these conditions, we observed that SIRT3 is required to regulate mitochondrial radical production and mitochondrial membrane potential, eventually leading to decreased neurodegeneration *in vitro* and in a fruit fly model of HD. Additionally, we provide evidence that SIRT3 fine-tunes the mitochondrial network structure and distribution in HD models rather than increasing mitochondrial mass, thereby supporting overall bioenergetics in neuronal cells.

Materials and Methods

Table I: Reagents and resources.

Reagent or Resource	Source	Catalog no./Identifier
Experimental models		
Tg(YAC128)53Hay mice	Slow *et al*. 2003	
FVB/NJ mice	Jackson Laboratory	001800
STHdh7/7, clone 2aA5	Coriell Institute	RRID: CVCL_M590
HTT93Q fruit flies	Steffan *et al.* 2001	
STHdh111/111, clone 109-1A	Coriell Institute	RRID: CVCL_M591
HD lymphoblasts	Coriell Institute	GM05622; GM04288; GM05678; GM05610; GM04724
CTR lymphoblasts	Coriell Institute	GM05724; GM04792; GM04800; GM04808
HD-iPSCs	Parker *et al.* 2008	
AMS-iPSCs	Onofre et al. 2016	
Antibodies		
β-actin (anti-mouse) 1:5000	Sigma-Aldrich	Cat# A5316
SDHA (anti-mouse) 1:5000	Molecular Probes	Cat# A11142
Drp1 (anti-mouse) 1:300	BD Biosciences	Cat# 611112
Fis1 (TTC11) (anti-rabbit) 1:1000	Novus Biologicals	Cat# NB100-56646
SIRT3 (D22A3) (anti-rabbit) 1:500	Cell Signaling	Cat# 5490
SIRT1 (anti-mouse) 1:1000	Sigma-Aldrich	Cat# S5196
SIRT5 (anti-rabbit) 1:500	Abcam	Cat# ab13697
HPS60 (anti-mouse) 1:1000	Chemicon	Cat# MAB3844
TBP (anti-mouse) 1:1000	Abcam	Cat# ab51841
TFAM (anti-rabbit) 1:300	Abcam	Cat# ab49134
PGC-1α (anti-goat) 1:500	Santa Cruz Biotech.	Cat# sc-5816
SOD2 (anti-rabbit) 1:2500	Abcam	Cat# ab13533
SOD2, acetyl K68 (anti-rabbit) 1:500	Abcam	Cat# ab137037
Acetyl-lysine (anti-rabbit) 1:1000	Cell Signaling	Cat# 9441S
Mitofusin 2 (anti-rabbit) 1:1000(WB)/1:450(ICC)	Sigma-Aldrich	Cat# M6319
Opa1 (anti-mouse) 1:500	BD Biosciences	Cat# 612606
Alexa Fluor-647 donkey (anti-mouse)	Molecular Probes	Cat# A31571
Alexa Fluor-647 donkey (anti-rabbit)	Molecular Probes	Cat# A31573
Anti-mouse alkaline phosphatase conjugated	Thermo Fisher Sci.	Cat# 31320
Anti-rabbit alkaline phosphatase conjugated	Thermo Fisher Sci.	Cat# 31340
Plasmids and siRNAs		
GFP-tagged human SIRT3	Origene	Cat# RG217770
pCMV-AC-GFP	Origene	Cat# PS100010
pDsRed2-Mito	Clontech	Cat# 632421
SIRT3 mouse siRNA silencer s82219 (#1)	Life Technologies	Cat# 4390771
SIRT3 mouse siRNA silencer s82220 (#2)	Life Technologies	Cat# 4390771
Silencer select negative control #1	Life Technologies	Cat# 4390843

Chemicals, Peptides, and Recombinant Proteins		
Hibernate E medium	Thermo Fisher Sci.	Cat# 1247601
Fatty acid free Bovine Serum Albumine (BSA)	Sigma-Aldrich	Cat# A8806
Glutamine	Sigma-Aldrich	Cat# G7513
Gentamicin	Thermo Fisher Sci.	Cat# 15750060
5-Fluoro-2′-deoxyuridine	Sigma-Aldrich	Cat# F0503
Gentamicin	Thermo Fisher Sci.	Cat# 10131027
Penicillin-Streptomycin	Thermo Fisher Sci.	Cat# 15140122
Fetal Bovine Serum	Alfagene	Cat# 10270106
Lipofectamine™ 3000	Sigma-Aldrich	Cat# L3000015
Soybean	Sigma-Aldrich	Cat# T9128
B-27™ Supplement (50X), serum free	Thermo Fisher Sci.	Cat# 17504044
Trypsin from porcine pancreas	Sigma-Aldrich	Cat# T4799
Viniferin	Sigma-Aldrich	Cat# SMB00074
PureZOL™ RNA Isolation Reagent	Bio-Rad	Cat# 7326880
Diethyl pyrocarbonate	Sigma-Aldrich	Cat# D5758
Oligomycin A	Sigma-Aldrich	Cat# 75351
Carbonyl cyanide 4-(trifluoromethoxy)phenylhydrazone (FCCP)	Sigma-Aldrich	Cat# C2920
Antimycin A	Sigma-Aldrich	Cat# A8674
Rotenone	Sigma-Aldrich	Cat# R8875
Hoechst 33342	Sigma-Aldrich	Cat# 14533
Propidium iodide	Sigma-Aldrich	Cat# P4170
Tetramethylrhodamine, Methyl Ester, Perchlorate (TMRM)	Thermo Fisher Sci.	Cat# T668
MitoSOX™ Red	Thermo Fisher Sci.	Cat# M36008
MitoTracker™ Deep Red FM	Thermo Fisher Sci.	Cat# M22426
Mitochondria peroxy yellow 1 (MitoPY1)	Tocris Bioscience	Cat# 4428
MitoTEMPO (MitoT)	Sigma-Aldrich	Cat# SML0737
TEMPOL	Sigma-Aldrich	Cat# 176141
Mowiol 40-88	Sigma-Aldrich	Cat# 324590
2-Mercaptoethanol	Sigma-Aldrich	Cat# M6250
MEM Non-essential Amino Acid solution	Thermo Fisher Sci.	Cat# M7145
FGF2 (Human) Recombinant Protein	Tebu-Bio	Cat# P3596
Commercial Assays		
Nuclear/Cytosol Fractionation Kit	BioVision	Cat# K266-100
NZY First-Strand cDNA Synthesis Kit	Nzytech	Cat# MB125
SsoFast Eva Green Supermix	Bio-Rad	Cat# 172-5201
iQ™ SYBR® Green Supermix	Bio-Rad	Cat# 1708880
PureLink™ Genomic DNA Mini Kit	Thermo Fisher Sci.	Cat# K182001
SIRT3 activity assay kit (fluorometric)	Abcam	Cat# ab156067
Culture Media		
DMEM - high glucose	Thermo Fisher Sci.	Cat# D5648
DMEM - basic	Thermo Fisher Sci.	Cat# D5030
Opti-MEM Reduced Serum Medium	Thermo Fisher Sci.	Cat# 31985062

KnockOut™ Serum Replacement	Thermo Fisher Sci.	Cat# 10828028
DMEM/F-12	Thermo Fisher Sci.	Cat# 11320033
RPMI-1640	Thermo Fisher Sci.	Cat# 11875093
Software		
Prism 8	Graphpad	https://www.graphpad.com/scientific-software/prism/
Fiji is just ImageJ	NIH	https://fiji.sc/
Image Lab	Bio-Rad	http://www.bio-rad.com/en-pt/product/image-lab-software
CFX qPCR Maestro Software	Bio-Rad	http://www.bio-rad.com/en-pt/category/qpcr-analysis-software
Seahorse Wave Controller	Agilent	
ZEN 2011 (black edition) software	Zeiss	https://www.micro-shop.zeiss.com/en/us/system/zen+software-software+zen-software/6008/
Other		
Seahorse XF24 cell culture microplates	Agilent	Cat# 102340-100

Human samples and ethical permits

Caudate and parietal cortex samples from 6 unaffected controls and 8 HD patients (Vonsattel grade II-III) (Table II) were obtained from German Brain Bank "Neurobiobank München" (http://www.neurobiobank.org). The postmortem intervals did not exceed 22 h. The ethical permit to use human samples was approved by Institutional Review Board from Faculty of Medicine, University of Coimbra, by 21 December 2015 (reference no. CE-136/2015).

Table II: Human sample identification, age (in years, y) and *postmortem* time (in hours, h).

Sample ID	Age (y)	*postmortem* time (h)
HD1 (parietal cortex only)	60.75	10
HD2 (parietal cortex and caudate)	38.58	10
HD3 (parietal cortex and caudate)	54	5.5
HD4 (parietal cortex only)	72.75	14.5
HD5 (parietal cortex and caudate)	56.92	4
HD6 (parietal cortex and caudate)	57.58	12
HD7 (parietal cortex only)	40.25	12
HD8 (parietal cortex and caudate)	68.75	20
CO1 (parietal cortex and caudate)	53.17	14.93
CO3 (parietal cortex and caudate)	59.5	11.57
CO4 (parietal cortex and caudate)	73	16.65
CO5 (parietal cortex and caudate)	51.58	20
CO6 (parietal cortex and caudate)	58.08	21.75
CO7 (caudate only)	53.17	14.97

Animals and ethical permits

Colonies of hemizygous YAC128 [line HD53] and wild-type (WT) mice, with FVB/N background, were housed in the Facility of the CNC, Coimbra, Portugal, under conditions of controlled temperature (22–23 °C) and under a 12-h light/12-h dark cycle. Food and water were available *ad libitum*. All mouse experiments were carried out in accordance with the guidelines of the Institutional Animal Care and Use of Committee and the European Community directive (2010/63/EU) and protocols approved by the Faculty of Medicine, University of Coimbra (ORBEA_189_2018/11042018).

Primary striatal neuron isolation, maintenance and transfection

Primary striatal neuronal cultures were generated from the offspring of crosses between WT mice (used as controls), or between hemizygous YAC128 male mice and WT females. Embryos from timed pregnant females were collected on day E15.5-16.5 of gestation. Striatum were dissected at 25 x magnification in ice-cold Hank's balanced salt solution (HBSS, 5.4 mM KCl, 0.4 mM KH_2PO_4, 137 mM NaCl, 4.2 mM $NaHCO_3$, 0.3 mM $NaH_2PO_4.H_2O$, 5 mM glucose, 5.4 mM sodium pyruvate, 5.4 HEPES) supplemented with 0.3 % fatty acid free BSA[18] and then transferred to Hibernate E medium for approximately 4 h or until the genotyping was concluded. Dissected tissue was pooled for each genotype and digested with HBSS supplemented with 0.003% trypsin. Soybean was used to block the trypsin. Neurons were cultured in Neurobasal medium supplemented with 2% B-27, 1 mM glutamine, 20 µg/ml gentamicin and plated at a density of 130 x 10^3 cells/cm^2 in poly-D-lysine (0.1 mg/ml)-coated plates. For low density cultures cells were plated at 85 x 10^3 cells/cm^2 on coverslips. Cultures were maintained at 37°C in a 5% CO_2 incubator and half of the medium was replaced after 3 days *in vitro* (DIV) with fresh supplemented Neurobasal medium containing 5-fluoro-2′-deoxyuridine (5 µM C_f) to inhibit glial division. Half of medium was replaced again with fresh medium at DIV7 and cells were used at DIV12/13.

In primary neurons, transfection with pDsRed2-Mito vector was performed at 8 DIV using the calcium phosphate precipitation method. Briefly, plasmid was diluted in TE (1 mM Tris-HCl pH 7.3, 1 mM EDTA), followed by the addition of $CaCl_2$ (2.5 M $CaCl_2$ in 10 mM HEPES, pH 7.2). The DNA solution was carefully added to 2 × HEBS (12 mM dextrose, 50 mM HEPES, 10 mM KCl, 280 mM NaCl and 1.5 mM $Na_2HPO_4.2H_2O$, pH 7.2) while bubbling air through the solution. The mixture was then incubated for 25 min at room temperature. The precipitates were added dropwise to the coverslips in Neurobasal medium and incubated for 80 min at 37°C. The DNA–Ca^{2+}-phosphate precipitates were dissolved in freshly-made dissolution medium (Neurobasal medium with 20 mM HEPES, pH 6.8) and incubated for 7 min at room temperature. The transfected neurons were then washed with Neurobasal medium and transferred back to their original dishes containing conditioned culture medium.

A working stock concentration of 10 mM viniferin was prepared in DMSO. Subsequent dilutions were done in culture media. 1 μM viniferin or DMSO (0.1%) was added 24 h before experiments.

Striatal cell culture conditions

Immortalized striatal neurons derived from knock-in mice expressing full-length normal (referred as Q7 or wild-type cells) or full-length mutant Htt (mHtt) with 111 glutamines (referred as Q111 or mutant cells) were obtained from Coriell Institute for Medical Research (USA) and maintained as previously described [19]. Cells were used until passage 16 by recommendation of cell line producer Dr M. MacDonald (Dept. of Neurology, Massachusetts General Hospital, Boston, USA). Transfection of striatal cells with selected plasmids or siRNAs (Table I) were performed with Lipofectamine™ 3000 transfection reagent accordingly to the manufacturer's instructions.

MitoTEMPO (MitoT; 2 μM) and TEMPOL (2 μM) were added and incubated for 24 h.

Human lymphoblastoid cell culture conditions

Human lymphoblastoid cell lines were obtained from Coriell Institute for Medical Research, derived from HD-affected patients containing heterozygous expansion mutation, four males (43/15, 45/15, 42/18, 49/17) and one female (47/18), or from unaffected voluntary control siblings, three males and one female, defined in this work as control (CTR) lymphoblasts. Cells were cultured in RPMI-1640 medium as previously described[16]. MitoTEMPO (MitoT; 2 μM) was added and incubated for 24 h.

Human induced pluripotent stem cell (iPSC) culture

Heterozygous human iPSC-HD4-iPS (XY) with 19/72 CAG repeats were generated by Park and colleagues [20] and kindly provided by Prof. George Daley (Harvard Medical School, Boston, Massachusetts, USA), whereas wild-type AMS4-iPS (XY) were generated by de Almeida and collaborators [21]. Cells were maintained on a layer of mitotically inactivated

murine embryonic fibroblasts (MEFs) for a variable number of passages or allowed to grow under feeder-free conditions on Geltrex® prior to experiments. MEFs were acquired from AMSBIO® inactivated or left to expand and further inactivated with mitomycin C after three passages. Manual dissection was routinely used to passage the cells. iPSCs were cultured in KSR media containing DMEM/F12 supplemented with 20% knockout serum replacement, 2 mM glutamine, 1 mM non-essential amino acids, 1% penicillin/streptomycin, 100 µM 2-mercaptoethanol and 10 ng/ml recombinant human FGF_2. Cultures were fed daily and passaged at least once a week.

Total, mitochondrial, nuclear and cytosolic-enriched fractions

Total fractions: Extracts were prepared in ice-cold lysis buffer (20 mM Tris, 100 mM NaCl, 2 mM EDTA, 2 mM EGTA, 50 mM NaF, 1 mM Na_3VO_4, 1% Triton; pH 7.4) supplemented with 1 mM 1,4- dithiothreitol (DTT), 100 µM phenylmethylsulfonyl fluoride (PMSF), 100 nM okadaic acid, 1 µg/mL protease inhibitor cocktail (chymostatin, pepstatin A, leupeptin, and antipain), 1 µM TSA (HDAC inhibitor) and 10 mM nicotinamide (SIRT inhibitor). In particular, for dot blotting assays, 0.05% Triton was used since higher concentrations can inhibit protein binding to the membrane. The homogenates (total fractions) were then frozen/thawed three times in liquid nitrogen and centrifuged at 20,800 x*g* for 10 min, at 4ºC, in order to remove cell debris; the resulting supernatant was collected and stored at -80ºC for later use.

Different fractions were obtained to evaluate protein levels of full length (FL-SIRT3), cleaved/activated mitochondrial SIRT3 (mSIRT3), and Drp1 in different compartments of the cells:

Mitochondrial- and cytosolic-enriched fractions: Cells were scraped or resuspended in ice-cold sucrose buffer (250 mM sucrose, 20 mM HEPES/KOH (pH 7.5), 100 mM KCl, 1.5 mM $MgCl_2$, 1 mM EGTA, and 1 mM EDTA), supplemented with 1 mM DTT, 100 µM PMSF, 100 nM okadaic acid, 1 µg/mL protease inhibitor cocktail, 1 µM TSA and 10 mM nicotinamide. Then, cells were homogenized with a Potter-Elvejhem 377 homogenizer with a Teflonpestle, at 300 rpm and centrifuged at 1,088 x*g* for 12 min (4ºC) to pellet the nuclei and cell debris. The supernatant was further centrifuged at 12,000 x*g* for 20 min (4ºC) and the resulting pellet

(mitochondrial-enriched fraction) resuspended in supplemented sucrose buffer. Trichloroacetic acid (15%) was added to the supernatant, and precipitated proteins were centrifuged at 16,300 *xg* for 10 min (4ºC). The resulting pellet (cytosolic-enriched fraction) was re-suspended in supplemented sucrose buffer and brought to pH 7 with KOH. Both protein extracts were stored at -80ºC for later use.

Nuclear-enriched fractions: Nuclear fractions were obtained using the Nuclear/Cytosol Extraction Kit from BioVision, following the manufacturer instructions. Briefly, cells were resuspended in in cytosol extraction buffer A containing DTT and proteases inhibitors and vigorously vortex for 15 sec. Extracts were then incubated on ice for 10 min. To remove the cytoplasmic fraction, ice-cold cytosol extraction buffer B was added to the cell suspension, and after a 5 sec vortex, centrifuged at 16,000 *xg* for 5 min (4ºC). The remaining pellet containing nuclei was resuspended in nuclear extraction buffer and vortex for 15 sec for every 10 min, for 40 min. The final extracts were centrifuged at 16,000 *xg* for 10 min (4ºC) and stored at -80ºC for later use.

Immunoblot analysis

Protein extracts were denatured with denaturing buffer (50 mM Tris-HCl pH 6.8, 2% SDS, 5% glycerol, 600 mM DTT, 0.01% bromophenol blue) at 95ºC, for 5 min. Equivalent amounts of protein (15-30 μg) were separated on an 8-12% SDS-PAGE and electroblotted onto polyvinylidene fluoride membranes (PVDF). For dot blotting, 5 μg total striatal extracts were directly applied onto a previously methanol-activated and equilibrated PVDF membrane. Membranes were blocked for 1 hour in Tris-buffered saline (TBS) solution containing 0.1% Tween (TBS-T) and 5% BSA, followed by an overnight incubation with primary antibodies listed in table I (at 4ºC) with gentle agitation. Membranes were then washed 3 times with TBS-T and incubated with secondary antibodies conjugated with alkaline phosphatase (1:20,000; 1 h) at room temperature, with gentle agitation. Immunoreactive bands were visualized by alkaline phosphatase activity after incubation with ECF substrate in a ChemiDoc Touch Imaging System (Bio-Rad). Bands were quantified using the Image Lab software.

mRNA extraction and qPCR

RNA from different samples was extracted with PureZOL RNA isolation reagent according to the manufacturer's protocol. Briefly, mice cortex was lysed after potter homogenization, whereas striatal cells, iPSCs and lymphoblasts were scraped or homogenized with a pipette. RNA was precipitated with isopropyl alcohol and the final pellet was resuspended with diethylpyrocarbonate 0.01% (v/v) water. The concentration of RNA was measured using a Nanodrop 2000 (ThermoScientific, Walthem, MA, USA) and the RNA integrity was confirmed by A260/280>1.9. RNA was transcribed into cDNA in a template–primer mix using the NZY First-Strand cDNA Synthesis kit (Nzytech, Portugal). The reaction was performed using a CFX96 qPCR system (Bio-Rad, Hemel Hempstead, UK) with the following steps: 5 min at 25°C, 30 min at 42°C and 5 min at 85°C. qPCR was performed using the SsoFast Eva Green Supermix or the iQTM SYBR® Green supermix (in the case of iPSC) using the following primers at 300 nM: human SIRT3 (forward: CGGCTCTACACGCAGAACATC; reverse: CAGCGGCTCCCCAAAGAACAC), human GAPDH (forward: 5'-ATTCCACCCATGGCAAATTC-3'; reverse: 5'-GGGATTTCCATTGATGACAAGC-3'), human tubulin (forward: 5'- CCAGGGCTGTGTTTGTAGACC-3'; reverse: 5'-CAATAGTGTAGTGTCCACGGGC-3'), human S18 (forward: 5'-GAGGATGAGGTGGAACGTGT-3'; reverse: 5' – TCTTCAGTCGCTCCACGTCT-3'), mouse SIRT3 (forward: 5'-GCCTGCAAGGTTCCTACTCC-3'; reverse: 5'-TCGAGGACTCAGAACGAACG-3') and mouse GAPDH (forward: 5'-CGGCCTTCCGTGTTCCATC-3'; reverse: 5'GAGTTGCTGTTGAAGTCGCA-3'). Amplification of 10 ng (50 ng for *SIRT3* mouse gene) template was performed with an initial cycle of 30 sec at 95ºC, followed by 40 cycles of 5 sec at 95ºC plus 5 sec at 59ºC (for cell extracts) or 61ºC (for tissue extracts). At the end of each cycle, Eva/SYBR Green fluorescence was recorded to enable determination of Cq. After amplification, the melting temperature of the PCR products was determined by performing melting curves, with 0.5ºC increments every 5 sec, from 65ºC to 95ºC, with fluorescence recorded after each temperature increment. For each set of primers amplification efficiency was assessed.

SIRT3 activity assay

SIRT3 activity was measured using the commercially available SIRT3 activity assay kit following the manufacture's' instructions. The assay is based in a fluorophore and quencher coupled to amino terminal and carboxyl terminal of a SIRT3 substrate peptide, respectively. When SIRT3 deacetylates the substrate peptide, this will be cut by the peptidase added simultaneously, separating the quencher and the fluorophore, and thus fluorescence is emitted. Briefly, two 100 mm^2 petri dish plates were used per condition to extract mitochondria using unsuplemented ice-cold sucrose buffer. After homogenization with a Potter-Elvejhem 377 homogenizer at 300 rpm, cell extract was centrifuged at 1,088 x*g* for 12 min (4ºC). The supernatant was further centrifuged at 12,000 x*g* for 20 min (4ºC) and the resulting mitochondrial-enriched pellet was resuspended in a provided SIRT3 assay buffer without supplements. The amount of protein was immediately quantified and 6 μg of mitochondria were distributed per well (in triplicates) in a black 96-well plate, containing fluoro-substrate peptide, peptidase and NAD^+. The fluorescence was monitored for 40 min at 1 min intervals using a microtiter plate reader fluorometer with excitation at 350 nm and emission at 450 nm. The rate of reaction was expressed as slope *per* min. As positive and negative controls, we used a recombinant SIRT3 provided by the kit and mitochondrial extracts of SIRT3 KD Q7 cells, respectively.

Lactate dehydrogenase (LDH) release assay

Striatal cells seeded in 12 well plates were transfected in Opti-MEM medium as previously described, and then medium was replaced by 300 µL regular high-glucose DMEM without phenol-red for 24 h. Culture medium was collected, and cells were scraped in 300 µL 10 mM HEPES (pH 7.4), 0.01% Triton X-100. Cell extracts were obtained by freeze-thaw cycles in liquid nitrogen. Both culture medium and extracts were centrifuged at 20,800 xg for 5 min (4°C) to remove cell debris. In a 96-well plate, the samples (in duplicates) were incubated with 1.58 mM pyruvate and 0.19 mM NADH. Extracellular and intracellular LDH was determined spectrophotometrically by following the rate of conversion for reduced

nicotinamide adenine dinucleotide to oxidized NAD^+, at 340 nm. The amount of released LDH in the medium was calculated using the ratio between extracellular/total LDH.

Oxygen consumption rate

OCR in striatal cells was measured using a Seahorse XFe-24 flux analyzer (Seahorse Bioscience, Billerica, MA, USA), following the manufacturer's instructions. Striatal cells were seeded in XF24 cell culture microplates at a density of 25,000 (Q7)/35,000 (Q111) cells per well. Prior to the experiments cells were washed, and culture medium was replaced by assay medium DMEM-5030 supplemented with 25 mM glucose and 2 mM glutamine, pH adjusted to 7.4, at 37°C. Four baseline measurements of OCR were sampled prior to sequential injection of mitochondrial complex V inhibitor oligomycin (1 μM), protonophore FCCP (1 μM) and antimycin A plus rotenone (1 μM each) to completely inhibit mitochondrial respiration. Accordingly, mitochondrial basal respiration, maximal respiration and ATP production was automatically calculated and recorded by the Seahorse software. Data was normalized for protein levels.

MitoSOX fluorescence

Striatal cells cultured on 18-mm coverslips were incubated in experimental media (in mM: 132 NaCl, 4 KCl, 1 $CaCl_2$, 1.2 $NaH_2PO_4.H_2O$, 1.4 $MgCl_2$, 6 Glucose, 10 HEPES, pH 7.4) supplemented with 1 μM MitoSOX red, 300 nM Mitotracker deep red and 1 μg/mL Hoechst 33342 for 25 min at 33ºC. Coverslips were washed and mounted in experimental media in a pre-warmed insert and images were collected using an Axio Observer Z1 system, a fully motorized inverted widefield microscope (Zeiss, Jena, Germany) equipped with a large stage incubator for temperature and humidity control and EC plan-neofluar/1.3NA 40x lens. MitoSOX fluorescence was imaged at 510 nm excitation and 580 nm emission. 20 images were collected per coverslip. Fluorescence intensities were calculated using Fiji software as previously described [22].

MitoPY1 fluorescence

Striatal cells were plated at a density of 25,000 (Q7)/35,000 (Q111) cells per well in 96-well assay plates and transfected with siRNA the following day. 48 h after transfection, cells were washed in experimental media and incubated for 40 min with 7 μM MitoPY1 at 37ºC and 5% CO_2. MitoPY1 fluorescence was imaged at 503 nm excitation and emission at 528 nm [23] using a Microplate Spectrofluorometer Gemini EM (Molecular Devices, USA). Basal levels were measured for 10 min followed by exposure to 2 μM antimycin A (AA), an inhibitor of mitochondrial complex III. Fluorescence was measured for an additional 30 min. The presented results are the slope of fluorescence after stimuli, normalized for protein content.

TMRM fluorescence

Striatal cells cultured on 18-mm coverslips were incubated in experimental media with 2 μg/ml Hoechst 33342 and 10 nM tetramethylrhodamine, methyl ester ($TMRM^+$), a concentration sufficient low to avoid quenching of the fluorescent signal in the matrix[24], for 30 min at 33°C. Coverslips were washed twice and mounted in a pre-warmed insert containing experimental media with 10 nM $TMRM^+$, and images were collected using LCI PlanNeofluar/1.3NA 63x lens on a Carl Zeiss Axio Observed Z1 inverted confocal microscope using the CSU-X1M spinning disc technology with Zen Black 2012 software (Zeiss, Jena, Germany). $TMRM^+$ fluorescence was monitored in a controlled temperature by excitation at 543 nm and emission at 458 nm, as described previously[25]. Four single positions were captured for each coverslip using the multi-position tiles tool. Images were collected every 10 sec with definite focus between each 6 cycles for a total of 54 cycles. Cells were exposed to 2.5 μg/mL oligomycin (cycle 18) and 2.5 μM FCCP (cycle 36) to induce $TMRM^+$ release from mitochondria. Fluorescence intensity at each time point was analyzed in Fiji software using the time series analyzer plugin (v 3.0) developed by Balaji J. (2007) at Dept. of Neurobiology, UCLA.

Mitochondrial network and co-localization studies

MitoDsRed- and GFP/SIRT3-GFP-transfected striatal cells were fixed with 4% paraformaldehyde (pre-warmed at 37°C) for 20 min, permeabilized in 0.1% Triton X-100 in PBS for 2 min and blocked for 1 hour, at room temperature in 3% (w/v) BSA in PBS. Anti-TFAM and anti-Drp1 primary antibodies were prepared in 3% (w/v) BSA in PBS and incubated overnight at 4°C. Nuclei were labelled with 4 µg/mL Hoechst 33342 for 20 min and mounted using Mowiol 40-88. Confocal images were obtained using a Plan-Apochromat/1.4NA 63x lens on an Axio Observer.Z1 confocal microscope (Zeiss Microscopy, Germany) with Zeiss LSM 710 software. Mitochondrial morphology and protein co-localization analysis was achieved using Macros designed by Doctor Jorge Valero (Center for Neuroscience and Cell Biology – University of Coimbra, presently at Achucarro – Basque Center for Neuroscience, Spain) in Fiji. Briefly, image background was normalized using the function Subtract Background, included in Fiji (rolling ball radius: 10 µm for mitochondria and proteins involved in mitochondrial dynamics; 30 µm for SIRT3- GFP/GFP, for 16-bit images). Mitochondria-targeting MitoDsRed images were extracted to grayscale. FindFoci function was then used to allow the identification of peak intensity regions[26] in order to show mitochondria-specific fluorescence. A threshold was applied to optimally resolve individual mitochondria. Mitochondrial outlines were traced through the Analyze Particles function. Aspect ratio (the ratio between the major and minor axis of mitochondria) was used as an index of mitochondrial length alongside Roundness (a relation between the area of mitochondria and its major axis). For proteins involved in mitochondrial dynamics a threshold was set similarly to the one described above, and Set Measurements function was employed to obtain Integrated Density (product of Area and Mean Gray Value) and later normalized to cellular area using the designed ROI area as an approximation. To obtain information about protein co-localization in mitochondria, a selection of mitochondrial ROIs was done, and the respective Integrated Density inside the ROIs was considered. SIRT3-GFP and GFP were analyzed in the same way, considering also the value of Integrated Density inside the nuclei. Each value derived represents a single cell.

mtDNA copy number

Genomic DNA was using Purelink genomic DNA kit according to the manufacturer's protocol. The concentration of gDNA was measured and 10 ng was used for each reaction. The mtDNA of each sample was amplified using sequence-specific primers to tRNATry/CO1 (forward: CAGTCTAATGCTTACTCAGC; reverse: GGGCAGTTACGATAACATTG), a gene region that is rarely deleted and contain only a few rare single nucleotide polymorphisms; whereas nuclear DNA (nDNA) was amplified using sequence-specific primers to beta-2-microglobulin (β2M). The reaction was performed using SsoFast Eva Green Supermix and thermal cycling conditions described above. mtDNA levels were expressed in relation to nDNA levels.

Mitochondrial movement analysis

MitoDsRed-transfected striatal neurons were washed and incubated in Na^+ medium (140 mM NaCl, 5 mM KCl, 1 mM $CaCl_2$, 1 mM $MgCl_2$, 10 mM Glucose, 10 mM HEPES, pH 7.4), and mitochondrial movement studies were carried out at 37°C. Neuron projections were imaged every 5 sec for a total of 145 frames, using a 63x objective with NA=1.4, on a Carl Zeiss Axio Observed Z1 inverted confocal microscope using CSU-X1M spinning disc. Mitochondrial movement analysis was done using the Kymograph Macro in Fiji (Rietdorf and Seitz, 2004). Briefly, histograms were matched to the first frame to correct fluorescence variations using Bleach Correction plugin developed by Miura and Rietdorf, and time lapse-dependent x-y drift was corrected applying TurboReg plugin. ROIs were designated using segmented line following mitochondria trajectory across projections. Kymographs generated in a x-y dimension (distance *vs* time) were used to obtain the slope to calculate mitochondrial velocity.

Apoptotic cell death

The nuclear morphology of the transfected striatal wild-type and mutant cells was analyzed by live fluorescence microscopy, using a double staining procedure with Hoechst 33342 and propidium iodide (PI). Following a washing step with Krebs medium, the cells mounted on 18-mm coverslips were incubated with 2 µg/ml Hoechst 33342 and 2 µg/ml PI for 10 min, at

33ºC. Cells were then washed 5 times in saline medium, in order to remove extracellular dyes, and further examined in an Axioskop 2 plus upright epi-fluorescence microscope (Zeiss, Jena, Germany) with PlanNeofluar/0.75NA 40x lens. Viable and apoptotic cells were counted in Fiji software using the Cell Counter plugin.

Drosophila husbandry and strains

Flies were raised on maize media, in LD12:12 at 25°C.The *elav-GAL4 [c155]* and the *mef2-GAL4* driver lines were obtained from the Bloomington Stock Centre, Indiana. The *w;UAS Htt93Q/CyO;+* flies were a gift from Larry Marsh and Leslie Thompson (University of California, Irvine) [27]. The *w;+;UAS dSirt2* line was a gift from Karen Chang (University of Southern California)[28]. Fly crosses were performed to generate a *Htt93Q dSirt2* line (genotype: *w; UAS Htt93Q/CyO; UAS dSirt2*). Experimental flies were generated by crossing *w;UAS Htt93Q/CyO;+* and *w; UAS Htt93Q/CyO; UAS dSirt2* flies to either *elav-GAL4* (for pan-neuronal expression) or *mef2-GAL4* (for expression in the muscles).

Fruit fly longevity assays

48 to 245 virgin females were collected for each experimental genotype and kept at 25°C in groups of 10 per vial. The number of surviving flies was scored in each vial on every day, and the flies moved to fresh food twice a week. Survival curve analysis were performed using the Log-rank (Mantel-Cox) test.

Rhabdomere quantification

The number of visible rhabdomeres per ommatidium was scored for 20 to 100 ommatidia per fly, with 16 to 26 flies examined per genotype at day 1 and 7 post-eclosion. Heads from aged flies were fixed to glass slides using fingernail polish, and rhabdomeres were examined at 40 x magnification using a Nikon Optiphot-2 microscope.

Statistical analysis

Results are expressed as the mean ± SEM (standard error of the mean) of the number of independent experiments or animals indicated in figure legends. Comparisons between multiple groups were performed by non-parametric one-way analysis of variance (ANOVA) using Kruskal-Wallis test. Correction for multiple comparisons was done by two-way ANOVA followed by Tukey post-hoc test. Comparison between two groups was performed by non-parametric Mann-Whitney test. For the analysis of life spam log-rank Mantel-Cox test was performed. The *F*-test was performed to analyze the interaction term. ROUT (Q=1%) method based on the false discovery rate was used to identify outliers. Significance was accepted at $p<0.05$. All statistical analyses were performed using Prism software (GraphPad Version 8.0).

Results

Mitochondrial SIRT3 levels and activity are increased in HD models and human caudate

Mitochondrial SIRT3 activity is regulated by distinct processes; in aging an overall decrease of its activity is well accepted, while during neurodegeneration data are not conclusive. Here we used several HD models, schematically represented in **Fig. 1**, and human post-mortem brain tissue from HD patients to characterize SIRT3 expression levels and activity. Knock-in striatal ST*Hdh*$^{Q111/Q111}$ cells expressing 111 CAG repeats in the chimeric human-mouse exon 1 of *HD* gene (hereafter Q111 cells) and cortical tissue isolated from YAC128 transgenic mice bearing 128 CAGs in the human *HD* gene presented a significant increase in SIRT3 mRNA levels ($p<0.01$ in striatal cells, $p<0.05$ in mice cortex (**Fig. 1b,f**). SIRT3 human and mouse transcripts codify proteins with a predicted molecular weight of 44 kDa and 36-37 kDa, respectively. They are cleaved by the MPP to become a 28 kDa enzymatically active mature form in the mitochondrial matrix [5,29]. Therefore, we evaluated both the full-length SIRT3 (FL-SIRT3) and processed enzymatically active mitochondrial SIRT3 (mSIRT3). The levels of processed mSIRT3 were also increased in Q111 cells ($p<0.05$) (**Fig. 1c**), while the inactive ~37 kDa FL-SIRT3 was reduced in cytosolic-enriched extracts ($p<0.05$) (**supplementary Fig. 1a**), suggesting increased translocation of SIRT3 to mitochondria in Q111 cells. Of note, we have not detected the enzymatic active form of endogenous mSIRT3 in cytosol of striatal cells (**supplementary Fig. 1a**). SIRT3 activity was also evaluated in mitochondrial-enriched extracts by the basic principle of a fluorophore and quencher coupled to an amino and carboxyl terminal of a SIRT3 acetylated substrate peptide in the presence of NAD^+. A pronounced increase in fluorescence over time was observed in Q111 in relation to Q7 wild-type cells ($p<0.001$) (**Fig. 1d**), correlating with increased substrate peptide cleavage. Recombinant SIRT3 and SIRT3 knockdown (KD) were used as positive and negative controls, respectively, to confirm the specificity of the reaction (**supplementary Fig. 1c**). In 12 month-old YAC128 brain cortex (late symptomatic) no significant differences were detected in SIRT3 protein levels (**Fig. 1g**), suggesting that increased SIRT3 may be an early adaptation. In the impossibility of studying SIRT3 activity in frozen tissue, we evaluated

acetylated levels of SOD2 at lysine 68 (k68), which has been described to be a primary target of SIRT3 [30]. Acetylated SOD2 was decreased in 12 month-old YAC128 compared to WT mouse cortex ($p<0.05$; **Fig. 1h**). This result can be interpreted as an indication of increased SIRT3 activity, and although the contribution of other classes of mitochondrial deacetylases for k68 acetylation are unlikely [30], the regulation of SOD2 activity by other acetylation sites cannot be ruled out.

As human models we used lymphoblasts derived from HD affected patients containing heterozygous expansion mutation (**Fig. 1i-l**) versus unaffected voluntary control siblings and HD patient-derived iPSC expressing either normal or 72 CAG-expanded form of *HD* gene (HD-iPSC) (**Fig. 1m-o**) versus AMS4-iPSC cells (Ctr-iPSC). HD lymphoblasts showed increased mRNA levels of SIRT3 ($p<0.01$), as well as increased mitochondrial SIRT3 protein levels ($p<0.001$) and activity ($p<0.05$) (**Fig. 1j-l**). FL-SIRT3 was detected in the nucleus, where it was described to interact with histones and transcriptional factors [3,4], but no changes in SIRT3 nuclei levels were detected between HD and Ctr lymphoblasts (**supplementary Fig. 1b**). HD-iPSC followed the same tendency, showing a significant increase in mitochondrial SIRT3 protein levels ($p<0.05$) and a trend for increased mRNA levels ($p=0.06$) (**Fig. 1n, o**).

To understand if the overall increase in SIRT3 activity observed in HD models also occurs in HD patients brains, samples from the two main regions affected in HD brain, caudate and parietal cortex, were tested from HD patients with grade II-III and non-affected controls. As observed previously in late-symptomatic HD mice, no significant changes were observed in SIRT3 levels in human postmortem HD tissues at late stage of the disease (**Fig. 2a, e**). Interestingly, when evaluating ac(K68)SOD2 as a substrate for SIRT3 (acSOD2/SIRT3 ratio), we observed a significant downregulation in HD caudate ($p<0.05$) but not in parietal cortex (**Fig. 2b, e**). Moreover, we detected a modest inverse correlation between SIRT3 and acSOD2 levels in HD caudate that was not observed in control samples (**Fig. 2c**). Remarkably, this inverse correlation was not detected in HD parietal cortex (**Fig. 2d**). Due to the delicate nature of the material and limited sample size it is rather precipitate to draw a definite conclusion about SIRT3 levels in human HD caudate; however, these data indicate

that decreased acSOD2 levels are associated with increased SIRT3 activity and that this increase is region specific. Different degrees of SIRT3 expression and activity were also found across the different HD models tested, which likely correlate with disease degree, the severity of the pathogenic mechanisms and oxidative stress.

SIRT3 regulates and is regulated by the oxidative status of HD cells

SIRT3 has been extensively described as a shield against oxidative stress and aging. Therefore, we hypothesized that increased activity of SIRT3 in HD cells may occur as a defense mechanism rather than a toxic response. To test how increased levels of SIRT3 affect mitochondrial oxidation in HD cells, we overexpressed SIRT3 in striatal cells and evaluated mitochondrial-derived ROS. Overexpression was confirmed by immunofluorescence (**Fig. 3a, b**) and immunoblotting (**supplementary Fig. 1d**). Interestingly, SIRT3-GFP colocalizes more in mitochondria (labelled with mitochondrial targeting sequence with an RFP tag, MitoDsRed) from Q111 than in Q7 cells as observed by the matching histogram (★) (**Fig 3b**). This accumulation of SIRT3 in HD mitochondria ($p<0.05$), occurs together with a decrease in nuclear location ($p<0.0001$) (**Fig. 3c**), supporting the data obtained for endogenous SIRT3 (**Fig. 1c**). Increased activity of SIRT3 was further confirmed in cellular extracts of SIRT3 overexpressing cells through decreased lysine acetylation, with no effects of GFP expression on acetyl-lysine levels (**Fig. 3d, supplementary Fig. 1e**).

Single cell levels of anion superoxide ($O_2^{\bullet-}$) were measured using the fluorescent probe MitoSOX. Q111 cells (transfected or GFP control) displayed exacerbated $O_2^{\bullet-}$ levels in comparison with Q7 cells ($p<0.001$) (**Fig. 3e, f**, **supplementary Fig. 2a, b**), as previously described by us [31]. As a proof-of-concept mitochondrial complex III inhibitor antimycin A (AA) and the mitochondrial or cytosolic ROS scavengers mitoTEMPO (MitoT) and TEMPOL, respectively, were used. MitoT significantly reduced mitochondrial $O_2^{\bullet-}$ levels in both non-treated and AA-treated Q111 cells ($p<0.0001$) (**supplementary Fig. 2a, b**), while TEMPOL was ineffective/non-significant, attesting the specific effect of MitoT on mitochondrial-derived ROS. In SIRT3 overexpressing Q111 cells, the levels of $O_2^{\bullet-}$ significantly dropped, by about

76%, reaching the levels of wild-type cells (**Fig. 3e, f**). Remarkably, MitoT showed no effect under SIRT3 overexpressing conditions, sustaining that SIRT3 acts as a stress sensitive enzyme to promote mitochondrial antioxidant activity in HD mutant cells. Instead, the knock down (KD) of SIRT3 in HD cells subjected to mitochondrial complex III inhibition increased the susceptibility of these cells to show increased mitochondrial ROS levels, without affecting cell viability (**supplementary Fig. 2c-e)**.

To ultimately show that SIRT3 constitutes a stress response protein in HD, we further treated striatal cells and human lymphoblasts with the antioxidant MitoT. While wild-type/control cells displayed stable levels of mSIRT3 after MitoT incubation, supporting a balanced oxidative environment, in MitoT-treated HD cells the levels of mitochondrial SIRT3 returned to the levels of control cells (**Fig. 3g**). These data indicate that mSIRT3 regulates and is regulated by the oxidant status of cells expressing mHTT,

SIRT3 prevents mitochondrial dysfunction in HD neural cells

Previously we have shown depolarization of mitochondria following excessive ROS levels in Q111 cells [33]. To understand if enhanced ROS scavenging achieved by SIRT3 overexpression in HD cells correlated with a healthy mitochondrial function, we evaluated mitochondrial membrane potential ($\Delta\psi_m$) using the membrane permeant cationic fluorescent probe $TMRM^+$ before and after mitochondria depolarization with FCCP in the presence of oligomycin (**Fig. 4a**). As described previously by us and others, Q111 striatal cells showed a decreased mitochondrial accumulation of $TMRM^+$ compared to wild-type cells, as observed by decreased probe release after FCCP ($p<0.01$) (**Fig. 4a-c**), reflecting decreased $\Delta\psi_m$. This decrease in $\Delta\psi_m$ may account for by impaired mitochondrial maximal respiration and ATP production observed in these cells ($p<0.05$) (**Fig. 4e, f**). SIRT3 overexpression in both Q7 and Q111 striatal cells led to more $TMRM^+$ accumulation, with a complete recovery of $\Delta\psi_m$ in mutant cells (**Fig. 4a-c**). Interestingly, SIRT3 KD decreased mitochondrial maximal respiration ($p<0.05$) but did not affect ATP production in Q111 cells (**Fig. 4e, f**), indicating that HD mitochondria still retained some metabolic reserve.

SIRT3 shapes mitochondrial network in HD striatal cells without affecting mitochondrial mass

To further address the mechanisms contributing for the improvement of mitochondrial bioenergetics prompt by SIRT3, we evaluated mitochondrial mass and the levels of the two major transcription factors influencing mitochondrial biogenesis and transcription, mitochondrial transcription factor A (TFAM) and its upstream regulator PGC-1α. Mutant cells showed decreased protein levels of PGC-1α ($p<0.001$) and TFAM ($p<0.05$) (**supplementary Fig. 3a, b, d**), accompanied by a substantial reduction in mitochondrial mass ($p<0.0001$) (**Fig. 4d)**. SIRT3 overexpression reestablished the levels of TFAM in mitochondria in HD mutant cells ($p<0.01$) to the levels of wild-type cells (**supplementary Fig. 3b, d**). Despite that, no significant changes in PGC-1α levels, mtDNA copy number or mitochondrial content were observed in SIRT3-overexpressing Q111 cells (**Fig. 4d, supplementary Fig. 4a, c**), indicating that the increase in TFAM levels is not sufficient to restore mitochondrial biogenesis in these cells.

ROS-mediated loss in $\Delta\psi_m$ is described to mediate mitochondrial fission [34]. Considering the preceding data, we speculated that SIRT3 may regulate mitochondrial dynamics. HD models are characterized by a large number of malfunctional small round-shaped mitochondria [35], which is partially related to the binding and hyperactivation of the mitochondrial fission GTPase dynamin-related protein 1 (Drp1) by mHTT [36]. Using mitochondrial and cytosolic-enriched extracts we confirmed that Q111 cells display Drp1 accumulation in mitochondria, compared to Q7 cells that have a more uniform distribution of Drp1 (**Fig. 5a**). Co-localization analysis of Drp1 with MitoDsRed corroborated the previous result (**supplementary Fig. 4a, b**), ultimately suggesting that mutant cells display increased fission, since Drp1 is a cytosolic protein that is only translocated to the outer mitochondrial membrane (OMM) to mediate mitochondrial constriction sites for fission, together with its adaptor Fis1 and endoplasmic reticulum [37]. Remarkably, analysis of the mitochondrial network revealed that both wild-type and mutant cells exhibit the three categories of mitochondrial network: fragmented, tubular or mixed (**Fig. 5b**). Both roundness, that indicates the degree of circularity, and aspect ratio, that positively correlates with length,

were analyzed for each independent cell to allow categorization of the mitochondrial network. Cells with roundness lower than 0.5 (or aspect ratio > 2.43; percentile 25%) were categorized as tubular, while cells with roundness higher than 0.55 (or aspect ratio < 2; percentile 75%) were categorized as fragmented, as demonstrated on **Fig. 5c**. Cells in between these cutoffs were considered as displaying mixed mitochondrial network. The uncoupler CCCP was used as a positive control for the fragmented network. Both values for aspect ratio and roundness fitted in the values obtained previously for the 'fragmented' category, validating the model (**supplementary Fig. 4c, d**). Cells displaying swollen mitochondria were discarded from this analysis, since they represented a minority of the whole population for either genotype (data not shown). Following the described categorization, we observed that Q111 cells show a substantial increase of fragmented mitochondria in detriment of tubular mitochondria (**Fig. 5d, e; supplementary Fig. 4e-g)**. Remarkably, overexpression of SIRT3 significantly reduced the number of mutant cells with fragmented mitochondria ($p<0.01$ for roundness; $p<0.05$ for aspect ratio) to similar levels of GFP-expressing wild-type cells (**Fig. 5d, e, supplementary Fig. 4g**). This effect may be partially related to the decrease of Drp1 levels in mitochondria of mutant cells in the presence of SIRT3 ($p<0.05$) (**Fig. 5f**). Additionally, SIRT3 overexpression also reduced total levels of the Drp1 adaptor on OMM, Fis1 ($p<0.05$) (**Fig. 4g**). Contrarily, SIRT3 did not affect mitochondrial fusion markers mitofusin 2 and optic atrophy 1 (Opa1) levels (**supplementary Fig. 4h, i**), suggesting that SIRT3 primarily influences mitochondrial network through regulation of fission.

Overall, these data suggest that SIRT3 affects Drp1 relocation, circumventing mitochondrial fragmentation induced by mHTT.

ε-Viniferin, a SIRT3 activator, favors mitochondrial elongation and anterograde transport in transgenic HD striatal neurons

Previous work by the Bossy-Wetzel group have shown that restoration of mitochondrial fusion, either by impairing Drp1 enzymatic activity or inducing Mfn2 function, directly correlate with rescue of HD neurons from neuritic trafficking defects and cell death [36]. ε-Viniferin (Vini) is a resveratrol dimer that has been shown to improve mitochondrial function and

enhance the expression of mitochondrial homeostasis-related proteins through SIRT3 activation [17,38,39]. Here, we used primary neurons isolated from YAC128 mice embryos to evaluate the effect of ε-viniferin, and consequent SIRT3 activation, on mitochondrial morphology and movement in this HD model. The increase in mSIRT3 protein and mRNA levels were confirmed ($p<0.05$), whereas the levels of SIRT1 and SIRT5 remained unchanged with Vini incubation (1 μM, 24 h) (**Fig. 5h, supplementary Fig. 5a, b**), suggesting an effect of ε-viniferin towards SIRT3, among other members of the sirtuin family known to directly influence mitochondrial function. As in striatal cells, YAC128 neurons also showed more fragmented mitochondria (2.3 aspect ratio in relation to 2.8 aspect ratio in WT neurons), which was completely prevented after ε-viniferin treatment ($p<0.05$) (**Fig. 5i**). Striatal MitoDsRed-transfected neurons were imaged in a spinning disk confocal with 5 sec intervals; YAC128 striatal neurons had approximately 90% stationary mitochondria and only ~3.5% were detected to move towards synaptic terminals (**Fig. 5j, k**). Additionally, the low percentage of moving mitochondria moved slower in YAC128 striatal neurites compared to the wild-type controls (mean velocity of 35.4 μm/s in YAC128 neurons, compared to 60.5 μm/s in WT conditions) ($p<0.05$) (**Fig. 5m, video 1, 2**). After ε-viniferin treatment, the percentage of stationary mitochondria in YAC128 neurons reduced significantly to 60% ($p<0.001$), mainly favoring anterograde transport that displayed about 7.6-fold increase in comparison with YAC128 vehicle-treated striatal neurons ($p<0.001$) (**Fig. 5j, k**). Additionally, ε-viniferin reestablished mitochondrial velocity ($p=0.0533$) (**Fig. 5m, video 1-3**).

Together, these data indicate that ε-viniferin-induced SIRT3 expression completely reestablished mitochondrial neuritic elongation and trafficking in YAC128 neurons, an effect that has been previously described to be dependent on SIRT3 activation [38].

Human SIRT3 and its fly-ortholog *Sirt2* confer neuroprotection *in vitro* and *in vivo*

Finally, we explored if SIRT3 was able to mitigate cell death and neuronal degeneration that characterize most HD models. Q111 cells showed a 3.4-fold increase in apoptotic cell death, compared to Q7 cells, measured by nuclear condensation using Hoechst/PI co-staining (**Fig.**

6a, b). On the contrary, Q111 cells overexpressing human SIRT3 displayed a significant reduction in DNA condensation ($p<0.0001$), entailing a complete regularization of apoptotic mechanisms (**Fig. 6b**).

To ultimately verify if SIRT3 also had neuroprotective functions *in vivo* we took advantage of a widely used fruit fly model of HTT toxicity [27] and the GAL4/UAS system to direct expression of mHtt exon 1 fragment (Htt93Q) either pan-neuronally with an *elav-GAL4* driver or to muscles (which have a high mitochondrial load) with a *mef2-GAL4* driver (**Fig. 6c**). Pan-neuronal expression of mHtt results in an obvious loss of photoreceptor neurons (rhabdomeres) leading to a disorganization of ommatidia [40] – a robust readout of neurodegeneration. While mammalian sirtuin family is composed by seven different SIRTs, there are just five members of the Sir2 family in *Drosophila melanogaster*. dSirt2 presents the highest sequence homology with hSIRT3 (54% similarity), followed by hSIRT2 (49% similarity) (**Supplementary Fig. 6a**). Additionally, it was shown that uniquely amongst the *Drosophila* sirtuins dSirt2 is an important regulator of mitochondrial function that impacts on acetylation of OXPHOS subunits (hSIRT3 recognized targets) [41]. While dSirt2 is not localized to mitochondria, of the *Drosophila* sirtuins it appears to be most functionally similar to mammalian SIRT3. Taking this information into consideration, we overexpressed dSirt2 in the HD fly model and analyzed lifespan and the number of rhabdomeres. While no changes in lifespan were observed in *elavHtt93Q dSirt2* flies, compared to *elav Htt93Q* (**Supplementary Fig. 6b**), HD flies with muscle dSirt2 overexpression displayed a significant lifespan increase ($p<0.0001$), with an extended median survival of 1.5 days and a maximum lifespan of 18-days (**Fig. 6d**), highlighting the importance of SIRT3 for mitochondria health. Moreover, pan-neuronal expression of dSirt2 in *elav Htt93Q* flies led to a mean recovery of ~50% of rhabdomeres lost by day 7 ($p<0.0001$) (**Fig. 6e**). All together these results strongly suggest that hSIRT3/dSirt2 can act as an important modifier of neurodegeneration in HD.

Discussion

Mitochondrial deregulation is an early event that characterizes all HD models and HD patients [16,42–44]. Our group and others have previously shown that sirtuin-activation compounds enhance mitochondrial biogenesis and function *in vivo* and *in vitro*, ameliorating HD phenotype [16,45]. These effects are mainly driven by SIRT1 nuclear targets PGC-1α, forkhead box O3A (Foxo3a) and cAMP response element binding protein (CREB) transcriptional pathways [16,45,46]. Interestingly, human HD cybrids, a cell model in which the contribution of mitochondria from patients is separate from the nucleus, also exhibit mitochondrial-associated metabolic deficits, suggesting that targeting mitochondria itself could be a better and more direct strategy to mitigate these deficits. Within the sirtuin family, SIRT3 has been shown to regulate the majority of the mitochondrial acetylome [1]. Here we provide evidence that SIRT3 mediates neuroprotective effects against mHTT-induced cell toxicity *in vitro* and *in vivo* through regulation of mitochondrial-driven oxidative stress and mitochondrial morphofunction. We found that HD mouse and human models and caudate from HD patients show increased SIRT3 levels and/or activity in response to high levels of oxidative damage [31,33,47]. Remarkably, SIRT3 levels regularize to normal levels after mitochondrial directed-antioxidant treatment, corroborating the previous assumption. In fact, the observed increase is not detrimental. On the other hand, we showed that SIRT3 promotes the translocation of Drp1 from mitochondria to cytosol, reducing mitochondrial fission that is classically increased in HD, as confirmed in our models. This event may account for the recovery of mitochondrial function and distribution in HD neural cells, rather than the increase in mitochondrial biogenesis, preventing cell death and increasing lifespan.

Several circumstances seem to regulate SIRT3 expression in the central nervous system. A previous study from the Duan laboratory using the same HD striatal cells reported decreased levels of the processed active mSIRT3 isoform [17] after serum deprivation, while SIRT3 baseline levels have not been quantified. This study diverges from describing the increase in SIRT3 levels as a stress response, as we and others [48] have observed. Concordantly with our data, pharmacological interference with the mitochondrial electron transport chain using the complex III inhibitor antimycin A, which induces increased mitochondrial ROS

levels, upregulated SIRT3 transcript expression in hippocampal neurons [8]. SIRT3 mRNA levels were also increased in the presence of beta-amyloid peptide (Aβ), the aggregation-prone molecule that characterizes Alzheimer's disease pathology [49]. Moreover, mitochondrial SIRT3 was reported to be increased in neurons where NAD^+ was depleted following stimulation with NMDA [50]. Although most of these studies describe SIRT3 activation under acute stress, we have proven that SIRT3 is also upregulated in HD models undergoing chronic stress. In fact, this lasting chronic activation may explain why ROS levels remain increased in our HD cell model and why further SIRT3 activation is protective. This postulation is supported by experiments showing that the powerful mitochondrial-directed antioxidant MitoT significantly decreased ROS and SIRT3 levels, and its protective effect was disguised by SIRT3 overexpression in HD cells. Therefore, we consider that despite increased SIRT3 activity, HD cells need an additional stimulus to disrupt the oxidative steady state where they stand to recover mitochondrial homeostasis.

Oxidative damage is one of the main players that drives mitochondrial dysfunction and cell death. We have shown that an oxidative stimulus like H_2O_2 in striatal Q111 cells causes a significant impairment in $\Delta\psi_m$ and induces caspase-3 activation [33,51]. Recently, a well-designed study aimed to understand the role of SIRT3 in adaptive responses of neurons to metabolic and excitatory challenges. Similarly to what we observed here, the authors found that neurons lacking SIRT3 exhibited increased vulnerability to excitotoxic, oxidative and metabolic stress induced by glutamate, H_2O_2 and 3-nitropropionic acid (3-NP, an irreversible inhibitor of complex II), respectively [52]. SIRT3 knockout mice showed decreased survival after 7 days of 3-NP administration and rotarod performance was significantly impaired compared to wild-type mice. Here as well, we showed that SIRT3 is linked to the activation of lifespan mechanisms, as already described several years ago for nuclear SIRT1 and SIRT6 [53,54], since *d*Sirt2/SIRT3 expression extended survival in flies with high metabolic demand expressing mHtt. Authors also showed that mitochondria of these SIRT3 knockout mice exhibited decreased levels of ATP and swelling associated with calcium dyshomeostasis [52]. The decrease in ATP production is likely linked to alterations in the electrochemical gradient across the mitochondrial membrane as SIRT3 is tightly associated

with ATP5O under physiological conditions, but upon loss of membrane potential this attachment with ATP synthase is reduced [9]. Loss of $\Delta\psi_m$ in our HD cells was also recovered after SIRT3 overexpression. Besides the above described effects, the sustained increase in SIRT3 was previously described to enhance the expression of subunits of mitochondrial complexes such as cyt *c* oxidase subunit 2 and 4, enhancing cellular respiration [55]. In addition, two mass spectrometry assays identified several mitochondrial complex subunits that were hyperacetylated on two or more lysine residues in SIRT3 knockout mice, including complex I/NADH dehydrogenase 1α, 1β subcomplexes and flavoprotein 1, complex II/SDH flavoprotein and iron-sulfur subunits, and complex IV/cyt *c* oxidase subunits 4-7 [2,56].

The relationship between mitochondrial energy defects and mitochondrial dynamics was first explored in detail by the Bossy-Wetzel lab. The authors showed that while the drop in ATP is a quick response to 3-NP-mediated complex II inhibition, mitochondrial fission only occurred after a late dramatic rise in ROS levels [57]. Moreover, depletion of $\Delta\psi_m$ seems to be another trigger event for mitochondrial fission, recruiting Drp1 to constriction sites at the mitochondrial outer membrane [58]. Our data indicate that the increase in filamentous mitochondria observed after SIRT3 overexpression occurs together with the drop in ROS levels. In accordance, nitric oxide was shown to induce S-nitrosylation of Drp1, increasing its GTPase activity and mitochondrial fragmentation [59]. In primary cultured neurons expressing mHTT a significant increase in nitric oxide production was observed and correlated with increased S-nitrosylation of Drp1, whereas transfection with non-nitrosylatable Drp1 mutant abrogated excessive mitochondrial fragmentation and dendritic spine loss [60]. Similarly, ROS-mediated modification of reactive cysteine thiol to form cysteine sulfenic acid to increase the sulfenylation of Drp1 at Cys644 also induced mitochondrial fragmentation [61]. Concordantly, the antioxidant agent acetyl-L-carnitine was able to decrease levels of Drp1 [62]. Interestingly, SIRT3 may also directly modulate Drp1 activity since one acetylation site was recently found for Drp1 at K642. Hyperacetylation of Drp1 at this site was observed to induce its oligomerization and phosphorylation at the activating serine 616 site in cardiomyocytes, recruiting Drp1 to OMM and promoting cell death [63].

Evidences that inhibition of mitochondrial fission is sufficient to hinder neurodegeneration have been accumulating. An impeccably study performed by Mochly-Rosen lab showed that inhibition of Drp1 binding to its adaptor Fis1 using the heptapeptide P110, is enough to decrease ROS levels and inhibit the propagation of the inflammatory response and neuronal cell death in neurons expressing 73Q and in R6/2 HD neurons [64]. These studies further support that strategies aiming a more balanced mitochondrial dynamics like SIRT3 activation, likely contribute to cope with neurodegeneration and increase cell survival. Nevertheless, it remains a challenge to pharmacologically modulate this enzyme to further consider clinical studies. Several studies, including the present work, have resorted to the use of pharmacological modulators that are not selective for a certain deacetylase. Viniferin is a resveratrol dimer recently shown to activate SIRT1 [65], although we observed no changes in SIRT1 levels in our model. This pleotropic effect is not necessarily disadvantageous, provided that it only operates at a pathological level, however it is difficult to reconcile whether the observed effects are exclusively due to SIRT3 activation. In the same way, unselective inhibition of deacetylases can also elicit unexpected side effects. Therefore, future research on crystal structure of the catalytic core of sirtuins and on specific binding modes of molecules will be able to offer valuable information for the design of novel targeting strategies. This might be particularly beneficial when considering the antioxidant and neuroprotective role of SIRT3 in HD pathogenesis.

Funding

Support for this work was provided by grants from the 'Fundação para a Ciência e a Tecnologia' (FCT) (Grant: EXPL/BIM-MEC/2220/2013), 'Gabinete de Apoio à Investigação' (GAI) funded by Faculty of Medicine of the University of Coimbra and Santander Totta Bank, and 'Fundação Luso-Americana para o Desenvolvimento' (FLAD)—Life Science 2020, Portugal. L.N. was supported by FCT (Grant: SFRH/BD/86655/2012). S.C., V.E.C. and F.G were supported by the Medical Research Council, UK (Grant: MR/M013847/1). CNC is supported by the European Regional Development Fund (ERDF), through Centro 2020 Regional Operational Programme: project CENTRO-01-0145-FEDER-000012-HealthyAging2020, the COMPETE 2020-Operational Programme for Competitiveness and Internationalisation and Portuguese national funds via FCT – Fundação para a Ciência e a Tecnologia, I.P.: project POCI-01-0145-FEDER-007440.

Acknowledgements

We thank Prof. George Q. Daley (Faculty of Medicine, Harvard Medical School, Boston) and Prof. Luis Pereira de Almeida (Center for Neuroscience and Cell Biology, Coimbra) for kindly providing the HD and Ctr iPSCs lines, respectively. We also thank Prof. Michael R. Hayden (CMMT - University of British Columbia, Vancouver) for kindly providing the YAC128 mice. We thank the Microscope Imaging Center for Coimbra (MICC) for helping in imaging acquisition. Human brain tissue was obtained from the German Brain Bank "Neurobiobank München" (http://www.neurobiobank.org)".

Authors contributions

L. N., C.C., F.G. and A.C.R. were responsible for experimental designs, data interpretation, and writing of the paper. L.N. performed and analyzed most of the experiments. C.C. performed experiments in striatal cells and analyzed, interpreted and described mitochondrial network. S.C., V.E.C. and F.G. designed, performed and analyzed *Drosophila* data. L.F. performed experiments involving MitoT and protein expression in neuronal cultures. J.V. designed and parameterized the macro for mitochondrial network and co-

localizations. C.L. performed and analyzed data on iPSCs. T.R.R. participated in results discussion. T.R.R., A.C.R. and F.G. provided funds. All authors read and approved the final manuscript.

References

[1] D.B. Lombard, F.W. Alt, H.-L.H.-L. Cheng, J. Bunkenborg, R.S. Streeper, R. Mostoslavsky, J. Kim, G. Yancopoulos, D. Valenzuela, A. Murphy, Y. Yang, Y. Chen, M.D. Hirschey, R.T. Bronson, M. Haigis, L.P. Guarente, R. V. Farese, S. Weissman, E. Verdin, B. Schwer, Mammalian Sir2 homolog SIRT3 regulates global mitochondrial lysine acetylation., Mol. Cell. Biol. 27 (2007) 8807–14. https://doi.org/10.1128/MCB.01636-07.

[2] A.S. Hebert, K.E. Dittenhafer-Reed, W. Yu, D.J. Bailey, E.S. Selen, M.D. Boersma, J.J. Carson, M. Tonelli, A.J. Balloon, A.J. Higbee, E. Al., Calorie restriction and SirT3 trigger global reprogramming of the mitochondrial protein acetylome, Mol. Cell. 49 (2013) 186–199.

[3] M.B. Scher, A. Vaquero, D. Reinberg, SirT3 is a nuclear NAD+-dependent histone deacetylase that translocates to the mitochondria upon cellular stress, Genes Dev. 21 (2007) 920–928. https://doi.org/10.1101/gad.1527307.

[4] T. Iwahara, R. Bonasio, V. Narendra, D. Reinberg, SIRT3 functions in the nucleus in the control of stress-related gene expression., Mol. Cell. Biol. 32 (2012) 5022–34. https://doi.org/10.1128/MCB.00822-12.

[5] B. Schwer, B.J. North, R.A. Frye, M. Ott, E. Verdin, The human silent information regulator (Sir)2 homologue hSIRT3 is a mitochondrial nicotinamide adenine dinucleotide-dependent deacetylase, J. Cell Biol. 158 (2002) 647–657. https://doi.org/10.1083/jcb.200205057.

[6] K. Brown, S. Xie, X. Qiu, M. Mohrin, J. Shin, Y. Liu, D. Zhang, D.T. Scadden, D. Chen, SIRT3 reverses aging-associated degeneration, Cell Rep. 3 (2013) 319–327. https://doi.org/10.1016/j.celrep.2013.01.005.

[7] J.L. Barger, J.M. Vann, N.L. Cray, T.D. Pugh, A. Mastaloudis, S.N. Hester, S.M. Wood, M.A. Newton, R. Weindruch, T.A. Prolla, Identification of tissue-specific transcriptional markers of caloric restriction in the mouse and their use to evaluate caloric restriction mimetics, Aging Cell. 16 (2017) 750–760. https://doi.org/10.1111/acel.12608.

[8] H.J.M. Weir, T.K. Murray, P.G. Kehoe, S. Love, E.M. Verdin, M.J. O'Neill, J.D. Lane, N. Balthasar, CNS SIRT3 expression is altered by reactive oxygen species and in

Alzheimer's disease., PLoS One. 7 (2012) e48225. https://doi.org/10.1371/journal.pone.0048225.

[9] W. Yang, K. Nagasawa, C. Münch, Y. Xu, K. Satterstrom, S. Jeong, S.D. Hayes, M.P. Jedrychowski, F.S. Vyas, E. Zaganjor, V. Guarani, A.E. Ringel, S.P. Gygi, J.W. Harper, M.C. Haigis, Mitochondrial Sirtuin Network Reveals Dynamic SIRT3-Dependent Deacetylation in Response to Membrane Depolarization, Cell. 167 (2016) 985-1000.e21. https://doi.org/10.1016/j.cell.2016.10.016.

[10] P. Onyango, I. Celic, J.M. McCaffery, J.D. Boeke, A.P. Feinberg, SIRT3, a human SIR2 homologue, is an NAD- dependent deacetylase localized to mitochondria, Proc. Natl. Acad. Sci. 99 (2002) 13653–13658. https://doi.org/10.1073/pnas.222538099.

[11] A. Cheng, Y. Yang, Y. Zhou, C. Maharana, D. Lu, W. Peng, Y. Liu, R. Wan, K. Marosi, M. Misiak, V.A. Bohr, M.P. Mattson, Mitochondrial SIRT3 Mediates Adaptive Responses of Neurons to Exercise and Metabolic and Excitatory Challenges, Cell Metab. (2015) 1–15. https://doi.org/10.1016/j.cmet.2015.10.013.

[12] X. Zhang, X. Ren, Q. Zhang, Z. Li, S. Ma, J. Bao, Z. Li, X. Bai, L. Zheng, Z. Zhang, S. Shang, C. Zhang, C. Wang, L. Cao, Q. Wang, J. Ji, PGC-1α/ERRα-Sirt3 Pathway Regulates DAergic Neuronal Death by Directly Deacetylating SOD2 and ATP Synthase β, Antioxid. Redox Signal. 24 (2016) 312–328. https://doi.org/10.1089/ars.2015.6403.

[13] Y. Liu, A. Cheng, Y.-J. Li, Y. Yang, Y. Kishimoto, S. Zhang, Y. Wang, R. Wan, S.M. Raefsky, D. Lu, T. Saito, T. Saido, J. Zhu, L.-J. Wu, M.P. Mattson, SIRT3 mediates hippocampal synaptic adaptations to intermittent fasting and ameliorates deficits in APP mutant mice, Nat. Commun. 10 (2019) 1886. https://doi.org/10.1038/s41467-019-09897-1.

[14] J. Lee, Y. Kim, T. Liu, Y.J. Hwang, S.J. Hyeon, H. Im, K. Lee, V.E. Alvarez, A.C. McKee, S.-J. Um, M. Hur, I. Mook-Jung, N.W. Kowall, H. Ryu, SIRT3 deregulation is linked to mitochondrial dysfunction in Alzheimer's disease, Aging Cell. 17 (2018) e12679. https://doi.org/10.1111/acel.12679.

[15] M.F. Beal, E. Brouillet, B.G. Jenkins, R.J. Ferrante, N.W. Kowall, J.M. Miller, E. Storey, R. Srivastava, B.R. Rosen, B.T. Hyman, Neurochemical and histologic characterization of striatal excitotoxic lesions produced by the mitochondrial toxin 3-nitropropionic acid.,

J. Neurosci. 13 (1993) 4181–4192.

[16] L. Naia, T.R. Rosenstock, A.M. Oliveira, S.I. Oliveira-Sousa, G.L. Caldeira, C. Carmo, M.N. Laço, M.R. Hayden, C.R. Oliveira, A.C. Rego, Comparative Mitochondrial-Based Protective Effects of Resveratrol and Nicotinamide in Huntington's Disease Models, Mol. Neurobiol. 54 (2017). https://doi.org/10.1007/s12035-016-0048-3.

[17] J. Fu, J. Jin, R.H. Cichewicz, S.A. Hageman, T.K. Ellis, L. Xiang, Q. Peng, M. Jiang, N. Arbez, K. Hotaling, C.A. Ross, W. Duan, trans-(-)-ε-Viniferin increases mitochondrial sirtuin 3 (SIRT3), activates AMP-activated protein kinase (AMPK), and protects cells in models of Huntington Disease., J. Biol. Chem. 287 (2012) 24460–72. https://doi.org/10.1074/jbc.M112.382226.

[18] L. Naia, A.C. Rego, Isolation and Maintenance of Striatal Neurons, Bio-Protocol. 8 (2018). https://doi.org/10.21769/BioProtoc.2823.

[19] F. Trettel, D. Rigamonti, P. Hilditch-Maguire, V.C. Wheeler, A.H. Sharp, F. Persichetti, E. Cattaneo, M.E. MacDonald, Dominant phenotypes produced by the HD mutation in STHdh(Q111) striatal cells., Hum. Mol. Genet. 9 (2000) 2799–809. https://doi.org/citeulike-article-id:11622336\rdoi: 10.1093/hmg/9.19.2799.

[20] I.-H. Park, N. Arora, H. Huo, N. Maherali, T. Ahfeldt, A. Shimamura, M.W. Lensch, C. Cowan, K. Hochedlinger, G.Q. Daley, Disease-Specific Induced Pluripotent Stem Cells, Cell. 134 (2008) 877–886. https://doi.org/10.1016/j.cell.2008.07.041.

[21] I. Onofre, N. Mendonça, S. Lopes, R. Nobre, J.B. de Melo, I.M. Carreira, C. Januário, A.F. Gonçalves, L.P. de Almeida, Fibroblasts of Machado Joseph Disease patients reveal autophagy impairment, Sci. Rep. 6 (2016) 28220. https://doi.org/10.1038/srep28220.

[22] I.L. Ferreira, C. Carmo, L. Naia, S. I. Mota, A. Cristina Rego, Assessing Mitochondrial Function in In Vitro and Ex Vivo Models of Huntington's Disease, in: S. V. Precious, et al. (Eds.), Huntington's Dis. Methods Mol. Biol., Springer, 2018: pp. 415–442. https://doi.org/10.1007/978-1-4939-7825-0_19.

[23] B.C. Dickinson, V.S. Lin, C.J. Chang, Preparation and use of MitoPY1 for imaging hydrogen peroxide in mitochondria of live cells., Nat. Protoc. 8 (2013) 1249–59. https://doi.org/10.1038/nprot.2013.064.

[24] D.G. Nicholls, M.W. Ward, Mitochondrial membrane potential and neuronal glutamate excitotoxicity: mortality and millivolts., Trends Neurosci. 23 (2000) 166–74. http://www.ncbi.nlm.nih.gov/pubmed/10717676.

[25] A.C. Rego, S. Vesce, D.G. Nicholls, The mechanism of mitochondrial membrane potential retention following release of cytochrome c in apoptotic GT1-7 neural cells., Cell Death Differ. 8 (2001) 995–1003. https://doi.org/10.1038/sj.cdd.4400916.

[26] A.D. Herbert, A.M. Carr, E. Hoffmann, FindFoci: A Focus Detection Algorithm with Automated Parameter Training That Closely Matches Human Assignments, Reduces Human Inconsistencies and Increases Speed of Analysis, PLoS One. 9 (2014) e114749. https://doi.org/10.1371/journal.pone.0114749.

[27] J.S. Steffan, L. Bodai, J. Pallos, M. Poelman, a McCampbell, B.L. Apostol, a Kazantsev, E. Schmidt, Y.Z. Zhu, M. Greenwald, R. Kurokawa, D.E. Housman, G.R. Jackson, J.L. Marsh, L.M. Thompson, Histone deacetylase inhibitors arrest polyglutamine-dependent neurodegeneration in Drosophila., Nature. 413 (2001) 739–743. https://doi.org/10.1038/35099568.

[28] A.J. Griswold, K.T. Chang, A.P. Runko, M.A. Knight, K.-T. Min, Sir2 mediates apoptosis through JNK-dependent pathways in Drosophila, Proc. Natl. Acad. Sci. 105 (2008) 8673–8678. https://doi.org/10.1073/pnas.0803837105.

[29] Y. Yang, B.P. Hubbard, D.A. Sinclair, Q. Tong, Characterization of murine SIRT3 transcript variants and corresponding protein products, J. Cell. Biochem. 111 (2010) 1051–1058. https://doi.org/10.1002/jcb.22795.

[30] Y. Chen, J. Zhang, Y. Lin, Q. Lei, K.-L. Guan, S. Zhao, Y. Xiong, Tumour suppressor SIRT3 deacetylates and activates manganese superoxide dismutase to scavenge ROS., EMBO Rep. 12 (2011) 534–541. https://doi.org/10.1038/embor.2011.65.

[31] M. Ribeiro, A.C. Silva, J. Rodrigues, L. Naia, A.C. Rego, Oxidizing effects of exogenous stressors in Huntington's disease knock-in striatal cells-protective effect oflcystamine and creatine, Toxicol. Sci. 136 (2013) 487–499.

[32] J.M. Marcus, S.A. Andrabi, SIRT3 Regulation Under Cellular Stress: Making Sense of the Ups and Downs, Front. Neurosci. 12 (2018). https://doi.org/10.3389/fnins.2018.00799.

[33] M. Ribeiro, T.R. Rosenstock, A.M. Oliveira, C.R. Oliveira, A.C. Rego, Insulin and IGF-1 improve mitochondrial function in a PI-3K/Akt-dependent manner and reduce mitochondrial generation of reactive oxygen species in Huntington's disease knock-in striatal cells, Free Radic. Biol. Med. 74 (2014) 129–144. https://doi.org/10.1016/j.freeradbiomed.2014.06.023.

[34] P.H.G.M. Willems, R. Rossignol, C.E.J. Dieteren, M.P. Murphy, W.J.H. Koopman, Redox Homeostasis and Mitochondrial Dynamics, Cell Metab. 22 (2015) 207–218. https://doi.org/10.1016/j.cmet.2015.06.006.

[35] C. Carmo, L. Naia, C. Lopes, A.C. Rego, Mitochondrial dysfunction in huntington's disease, 2018. https://doi.org/10.1007/978-3-319-71779-1_3.

[36] W. Song, J. Chen, A. Petrilli, G. Liot, E. Klinglmayr, Y. Zhou, P. Poquiz, J. Tjong, M.A. Pouladi, M.R. Hayden, E. Masliah, M. Ellisman, I. Rouiller, R. Schwarzenbacher, B. Bossy, G. Perkins, E. Bossy-Wetzel, Mutant huntingtin binds the mitochondrial fission GTPase dynamin-related protein-1 and increases its enzymatic activity., Nat. Med. 17 (2011) 377–82. https://doi.org/10.1038/nm.2313.

[37] O.C. Losón, Z. Song, H. Chen, D.C. Chan, Fis1, Mff, MiD49, and MiD51 mediate Drp1 recruitment in mitochondrial fission, Mol. Biol. Cell. 24 (2013) 659–667. https://doi.org/10.1091/mbc.e12-10-0721.

[38] S. Zhang, Y. Ma, J. Feng, Neuroprotective mechanisms of ε-viniferin in a rotenone-induced cell model of Parkinson's disease: significance of SIRT3-mediated FOXO3 deacetylation, Neural Regen. Res. 15 (2020) 2143. https://doi.org/10.4103/1673-5374.282264.

[39] D. Kurundkar, A.R. Kurundkar, N.B. Bone, E.J. Becker, W. Liu, B. Chacko, V. Darley-Usmar, J.W. Zmijewski, V.J. Thannickal, SIRT3 diminishes inflammation and mitigates endotoxin-induced acute lung injury, JCI Insight. 4 (2019). https://doi.org/10.1172/jci.insight.120722.

[40] E.W. Green, F. Giorgini, Choosing and using Drosophila models to characterize modifiers of Huntington's disease, Biochem. Soc. Trans. 40 (2012) 739–745. https://doi.org/10.1042/BST20120072.

[41] M. Rahman, N.K. Nirala, A. Singh, L.J. Zhu, K. Taguchi, T. Bamba, E. Fukusaki, L.M.

Shaw, D.G. Lambright, J.K. Acharya, U.R. Acharya, Drosophila Sirt2/mammalian SIRT3 deacetylates ATP synthase β and regulates complex V activity., J. Cell Biol. 206 (2014) 289–305. https://doi.org/10.1083/jcb.201404118.

[42] J. Shehadeh, H.B. Fernandes, M.M. Zeron Mullins, R.K. Graham, B.R. Leavitt, M.R. Hayden, L.A. Raymond, Striatal neuronal apoptosis is preferentially enhanced by NMDA receptor activation in YAC transgenic mouse model of Huntington disease, Neurobiol. Dis. 21 (2006) 392–403. https://doi.org/10.1016/j.nbd.2005.08.001.

[43] I.L. Ferreira, T. Cunha-Oliveira, M. V. Nascimento, M. Ribeiro, M.T. Proença, C. Januário, C.R. Oliveira, A.C. Rego, Bioenergetic dysfunction in Huntington's disease human cybrids, Exp. Neurol. 231 (2011) 127–134. https://doi.org/10.1016/j.expneurol.2011.05.024.

[44] A.C. Silva, S. Almeida, M. Laço, A.I. Duarte, J. Domingues, C.R. Oliveira, C. Januário, A.C. Rego, Mitochondrial respiratory chain complex activity and bioenergetic alterations in human platelets derived from pre-symptomatic and symptomatic huntington's disease carriers, Mitochondrion. 13 (2013) 801–809. https://doi.org/10.1016/j.mito.2013.05.006.

[45] H. Jeong, D.E. Cohen, L. Cui, a Supinski, J.N. Savas, J.R. Mazzulli, J.R. Yates 3rd, L. Bordone, L. Guarente, D. Krainc, Sirt1 mediates neuroprotection from mutant huntingtin by activation of the TORC1 and CREB transcriptional pathway, Nat Med. 18 (2012) 159–165. https://doi.org/10.1038/nm.2559.

[46] M. Jiang, J. Wang, J. Fu, L. Du, H. Jeong, T. West, L. Xiang, Q. Peng, Z. Hou, H. Cai, T. Seredenina, N. Arbez, S. Zhu, K. Sommers, J. Qian, J. Zhang, S. Mori, X.W. Yang, K.L.K. Tamashiro, S. Aja, T.H. Moran, R. Luthi-Carter, B. Martin, S. Maudsley, M.P. Mattson, R.H. Cichewicz, C.A. Ross, D.M. Holtzman, D. Krainc, W. Duan, Neuroprotective role of Sirt1 in mammalian models of Huntington's disease through activation of multiple Sirt1 targets., Nat. Med. 18 (2012) 153–8. https://doi.org/10.1038/nm.2558.

[47] C. Hong, H. Seo, M. Kwak, J. Jeon, J. Jang, E.M. Jeong, J. Myeong, Y.J. Hwang, K. Ha, M.J. Kang, K.P. Lee, E.C. Yi, I.-G. Kim, J.-H. Jeon, H. Ryu, I. So, Increased TRPC5 glutathionylation contributes to striatal neuron loss in Huntington's disease., Brain. 138 (2015) 3030–47. https://doi.org/10.1093/brain/awv188.

[48] E. Buck, H. Bayer, K.S. Lindenberg, J. Hanselmann, N. Pasquarelli, A.C. Ludolph, P. Weydt, A. Witting, Comparison of Sirtuin 3 Levels in ALS and Huntington's Disease—Differential Effects in Human Tissue Samples vs. Transgenic Mouse Models, Front. Mol. Neurosci. 10 (2017). https://doi.org/10.3389/fnmol.2017.00156.

[49] M. Cieślik, G.A. Czapski, J.B. Strosznajder, The Molecular Mechanism of Amyloid β42 Peptide Toxicity: The Role of Sphingosine Kinase-1 and Mitochondrial Sirtuins., PLoS One. 10 (2015) e0137193. https://doi.org/10.1371/journal.pone.0137193.

[50] S.H. Kim, H.F. Lu, C.C. Alano, Neuronal sirt3 protects against excitotoxic injury in mouse cortical neuron culture, PLoS One. 6 (2011). https://doi.org/10.1371/journal.pone.0014731.

[51] M. Ribeiro, T.R. Rosenstock, T. Cunha-Oliveira, I.L. Ferreira, C.R. Oliveira, A.C. Rego, Glutathione redox cycle dysregulation in Huntington's disease knock-in striatal cells, Free Radic. Biol. Med. 53 (2012) 1857–1867. https://doi.org/10.1016/j.freeradbiomed.2012.09.004.

[52] A. Cheng, Y. Yang, Y. Zhou, C. Maharana, D. Lu, W. Peng, Y. Liu, R. Wan, K. Marosi, M. Misiak, V.A. Bohr, M.P. Mattson, Mitochondrial SIRT3 Mediates Adaptive Responses of Neurons to Exercise and Metabolic and Excitatory Challenges, Cell Metab. 23 (2016) 128–142. https://doi.org/10.1016/j.cmet.2015.10.013.

[53] Y. Kanfi, S. Naiman, G. Amir, V. Peshti, G. Zinman, L. Nahum, Z. Bar-Joseph, H.Y. Cohen, The sirtuin SIRT6 regulates lifespan in male mice, Nature. 483 (2012) 218–221. https://doi.org/10.1038/nature10815.

[54] K. Howitz, J. Bitterman, H. Cohen, Small molecule activators of sirtuins extend Saccharomyces cerevisiae lifespan, Nature. 425 (2003) 191–196. https://doi.org/10.1038/nature01965.1.

[55] T. Shi, F. Wang, E. Stieren, Q. Tong, SIRT3, a mitochondrial sirtuin deacetylase, regulates mitochondrial function and thermogenesis in brown adipocytes., J. Biol. Chem. 280 (2005) 13560–7. https://doi.org/10.1074/jbc.M414670200.

[56] M.J. Rardin, J.C. Newman, J.M. Held, M.P. Cusack, D.J. Sorensen, B. Li, B. Schilling, S.D. Mooney, C.R. Kahn, E. Verdin, B.W. Gibson, Label-free quantitative proteomics of the lysine acetylome in mitochondria identifies substrates of SIRT3 in metabolic

pathways, Proc. Natl. Acad. Sci. . 110 (2013) 6601–6606. https://doi.org/10.1073/pnas.1302961110.

[57] G. Liot, B. Bossy, S. Lubitz, Y. Kushnareva, N. Sejbuk, E. Bossy-Wetzel, Complex II inhibition by 3-NP causes mitochondrial fragmentation and neuronal cell death via an NMDA- and ROS-dependent pathway., Cell Death Differ. 16 (2009) 899–909. https://doi.org/10.1038/cdd.2009.22.

[58] W. Bleazard, J.M. McCaffery, E.J. King, S. Bale, A. Mozdy, Q. Tieu, J. Nunnari, J.M. Shaw, The dynamin-related GTPase Dnm1 regulates mitochondrial fission in yeast., Nat. Cell Biol. 1 (1999) 298–304. https://doi.org/10.1038/13014.

[59] D.-H. Cho, T. Nakamura, J. Fang, P. Cieplak, A. Godzik, Z. Gu, S.A. Lipton, S-Nitrosylation of Drp1 Mediates β-Amyloid-Related Mitochondrial Fission and Neuronal Injury, Science (80-.). 324 (2009) 102–105. https://doi.org/10.1126/science.1171091.

[60] F. Haun, T. Nakamura, A.D. Shiu, D.-H. Cho, T. Tsunemi, E.A. Holland, A.R. La Spada, S.A. Lipton, S-Nitrosylation of Dynamin-Related Protein 1 Mediates Mutant Huntingtin-Induced Mitochondrial Fragmentation and Neuronal Injury in Huntington's Disease, Antioxid. Redox Signal. 19 (2013) 1173–1184. https://doi.org/10.1089/ars.2012.4928.

[61] Y.-M. Kim, S.-W. Youn, V. Sudhahar, A. Das, R. Chandhri, H. Cuervo Grajal, J. Kweon, S. Leanhart, L. He, P.T. Toth, J. Kitajewski, J. Rehman, Y. Yoon, J. Cho, T. Fukai, M. Ushio-Fukai, Redox Regulation of Mitochondrial Fission Protein Drp1 by Protein Disulfide Isomerase Limits Endothelial Senescence, Cell Rep. 23 (2018) 3565–3578. https://doi.org/10.1016/j.celrep.2018.05.054.

[62] M. Morigi, L. Perico, C. Rota, L. Longaretti, S. Conti, D. Rottoli, R. Novelli, G. Remuzzi, A. Benigni, Sirtuin 3-dependent mitochondrial dynamic improvements protect against acute kidney injury., J. Clin. Invest. 125 (2015) 715–26. https://doi.org/10.1172/JCI77632.

[63] Q. Hu, H. Zhang, N.G. Cortés, D. Wu, P. Wang, E. Smith, M. Wang, S.-S. Sheu, W. Wang, Increased Drp1 Acetylation Mediates Lipid Overload-induced Cardiomyocyte Death And Heart Dysfunction, Circ. Res. 125 (2019). https://doi.org/10.1161/res.125.suppl_1.279.

[64] A.U. Joshi, P.S. Minhas, S.A. Liddelow, B. Haileselassie, K.I. Andreasson, G.W. Dorn,

D. Mochly-Rosen, Fragmented mitochondria released from microglia trigger A1 astrocytic response and propagate inflammatory neurodegeneration, Nat. Neurosci. 22 (2019) 1635–1648. https://doi.org/10.1038/s41593-019-0486-0.

[65] H. Zhao, T. Ma, B. Fan, L. Yang, C. Han, J. Luo, L. Kong, Protective effect of trans-δ-viniferin against high glucose-induced oxidative stress in human umbilical vein endothelial cells through the SIRT1 pathway, Free Radic. Res. 50 (2016) 68–83. https://doi.org/10.3109/10715762.2015.1108412.

Figure legends

Figure 1. Increased mitochondrial SIRT3 levels and activity in HD models.

(a) Schematic representation of striatal cells expressing 111 CAG repeats in chimeric human-mouse HD exon 1.

(b) SIRT3 mRNA levels in striatal cells were quantified by qPCR and normalized for GAPDH (n=5).

(c) Mitochondrial SIRT3 (mSIRT3) protein levels were quantified by western blotting in mitochondrial enriched-fractions from Q7 wild-type and Q111 knock-in mice striatal cells. Data was normalized for SDHA (n=7).

(d) SIRT3 activity was quantified in mitochondrial fractions by fluorometric assay (n=4).

(e) Schematic illustration of mouse brain emphasizing the cortical area used to obtain protein extracts (in blue), and respective expression of the yeast artificial chromosome (YAC) bearing 128 CAG repeats in the human *HD* gene.

(f) SIRT3 mRNA levels in cortical homogenates from 12-month-old YAC128 *vs* wild-type (WT) mice were quantified by qPCR and normalized for GAPDH (n=4).

(g, h) Cortical homogenates from 12-month-old YAC128 *vs* wild-type (WT) mice were tested for mSIRT3 and acetyl(K68)SOD2. Data were normalized for SDHA or total SOD2, respectively (n=4).

(i) Schematic representation of human heterozygous HD lymphoblasts expressing 42 to 49 CAG repeats in HD gene.

(j) SIRT3 mRNA levels in lymphoblasts were quantified by qPCR and normalized for GAPDH (n=3).

(k) mSIRT3 levels were quantified in mitochondrial-enriched lysates from affected HD human lymphoblasts or unaffected siblings. Data was normalized for HSP60 (n=4).

(l) SIRT3 activity was quantified in mitochondrial fractions from lymphoblasts by fluorometric assay (n=12).

(m) Schematic representation of a colony of human induced pluripotent stem cells (iPSCs) derived from a heterozygous HD patient expressing 72 CAG repeats in HD gene.

(n) SIRT3 mRNA levels in iPSC were quantified by qPCR and normalized for actin (n=4-6).

(o) mSIRT3 levels were analyzed in total extracts from HD-iPSCs or unaffected controls (CTR-iPSC). Data was normalized for actin (n=3).

Statistical significance: $^{*}p<0.05$, $^{**}p<0.01$, $^{***}p<0.001$ by non-parametric Mann-Whitney test; n.s.=non-significant.

Figure 2. Inverse correlation between mitochondrial SIRT3 and acSOD2 levels is specific of human HD caudate.

(a, b) mSIRT3 and acetyl(K68)-SOD2 (normalized for its deacetylase activator SIRT3) were quantified by western blotting in total extracts from post-mortem samples from caudate and parietal cortex of control (Ctr) and HD patients (grade II-III). Violin plots show median, 25th and 75th percentile and minimum and maximum values, whereas plots represent independent individuals (n=5-6 for caudate; n=5-8 for cortex).

(c, d) Pearson correlation was done between SIRT3 *vs* acSOD2 protein levels.

(e) Representative blots of the a, b quantifications (caudate samples in left panel and parietal cortical samples in right panel).

Statistical significance: $^{*}p<0.05$ by non-parametric Mann-Whitney test.

Figure 3. Overexpressed SIRT3 accumulates more in HD mitochondria and blocks ROS production.

(a, b) Confocal images of Q7 or Q111 cells expressing MitoDsRed and SIRT3-GFP. Scale bar = 3 µm. Highlighted boxes show regions at higher magnification. In **b**, several SIRT3-GFP stained regions are associated with mitochondria (white arrow heads). The graphs on the right represent relative fluorescence intensity of MitoDsRed and SIRT3-GFP. Note that while in Q7 cells (in **a**) SIRT3-GFP fluorescence peaks do not match with those of MitoDsRed, in Q111 cells (in **b**) SIRT3-GFP peaks frequently coincide with peaks of MitoDsRed fluorescence (indicated by stars).

(c) SIRT3-GFP cellular distribution was quantified considering its co-localization with MitoDsRed and Hoechst 33342, as described in material and methods (n=3, measured in ~25 cells/condition). 2-way ANOVA analysis revealed an interaction between genotype and SIRT3-GFP cellular distribution $F(2,468)=20.67$ ($p<0.0001$).

(d) Total lysine acetylation was evaluated by dot blotting using an acetyl-lysine antibody.

(e-f) GFP and SIRT3-GFP transfected cells were treated, when indicated with antioxidant mitoTEMPO (MitoT; 2 µM, 24 h) and single-cell MitoSox Red fluorescence was imaged and quantified (n=3, considering ~35 cells/condition). 2-way ANOVA reveals an effect of genotype $F(1,208)=5.172$ ($p<0.05$), treatment $F(2,208)=17.69$ ($p<0.0001$) and an interaction between both $F(2,208)=60.07$ ($p<0.0001$). Scale bar = 10 µm.

(g) Striatal cells and human lymphoblasts were either treated with MitoTEMPO (MitoT; 2 μM, 24 h) or left untreated and SIRT3 levels were quantified in mitochondrial extracts (n=3). Representative blots follow the sequence of the bar graphs. 2-way ANOVA revealed an effect of genotype in striatal cells $F(1,17)=5.489$ ($p<0.032$) and an effect of MitoT treatment in lymphoblasts $F(1,16)=23.33$ ($p=0.0002$).

Statistical significance: $^{*}p<0.05$, $^{**}p<0.01$, $^{****}p<0.0001$ ordinary two-way ANOVA, followed by Tukey post-hoc test. ns=non-significant.

Figure 4. SIRT3 stimulates mitochondrial bioenergetics without affecting mitochondrial content.

(a-c) Mitochondrial membrane potential was measured using $TMRM^{+}$ in non-quenching conditions). Units of fluorescence (calibration bar) were monitored before and after exposure to 2 μM FCCP. Release of $TMRM^{+}$ after depolarization is presented in **b** and quantified in **c** (n=4-5, considering 10-35 cells/condition). 2-way ANOVA analyses shows a significant effect of both genotype [$F(1,151)=8.528$; $p=0.0040$] and SIRT3 overexpression [$F(1,151)=10.53$; $p=0.0014$]. Scale bar: 10 μm.

(d) Mitochondria were labeled using targeted DsRed. The percentage of cell area occupied by mitochondria was quantified in Image J, measured in ~20 cells/condition.

(e-f) Oxygen consumption rate (OCR) was evaluated by Seahorse analyzer in SIRT3 KD (using two different siRNAs) or scramble control cells. Basal respiration, maximal respiration and oligomycin-dependent ATP production were calculated relative to the control Q7 scramble (n=5-8). The dashed line indicates the OCR value for Q7 scramble. An effect of genotype was detected for basal respiration [$F(1,28)=19.56$; $p=0.0001$], maximal respiration [$F(1,28)=39.42$; $p<0.0001$] and ATP production [$F(1,28)=24.52$; $p<0.0001$]. SIRT3 KD showed an effect on maximal respiration [$F(2,28)=3.716$; $p=0.0375$].

Statistical significance: $^{*}p<0.05$ (*vs* Q7 scramble)**,** $^{\#}p<0.05$ (*vs* Q111 scramble) $^{**}p<0.01$, $^{****}p<0.0001$ by ordinary 2-way ANOVA Tukey's multiple comparations test.

Figure 5. Induced SIRT3 expression modulates Drp1 fission protein and re-establishes mitochondrial network and trafficking.

(a) Protein levels of Drp1 were assessed in mitochondrial-enriched and cytosolic fractions by western blotting in untransfected cells (n=3).

(b, c) Mitochondria were labeled using targeted DsRed and selected images are representative of a population of cells exhibiting mainly fragmented or tubular mitochondria,

or a mix of both. Percentile analysis of the roundness of mitochondria was used for categorization of mitochondrial morphology. Scale bar: 10 μm.

(d, e) GFP and SIRT3-GFP expressing striatal cells were classified accordingly by roundness of their mitochondria established in **c**, and quantification represented in **e** (n=3/4, in ~20 cells/condition). Scale bar: 10 μm. Two-way ANOVA indicated a interaction between genotype and mitochondrial morphology [F(2,24)=11.44; p=0.0003].

(f) Drp1 co-localization with mitochondria was quantified by ICC (n=3, in ~30 cells/condition). Two-way ANOVA revealed an effect of genotype [F(1,491)=9.421; p=0.0023] and an interaction between genotype and SIRT3 overexpression [F(1,491)=4.45; p=0.0354].

(g) Fis1 protein levels were assessed in total protein extracts by western blotting. Representative blot follows the sequence of graph bars. Data is presented as the mean ± SEM of 7 independent experiments. Two-way ANOVA analysis revealed an effect of genotype [F(1,30)=5.306; p=0.0284] and an effect of SIRT3 overexpression [F(1,30)=10.48; p=0.0029].

(h) YAC128 and WT primary striatal neurons were treated with DMSO (Veh) or Viniferin (Vini, 1 μM) for 24 h. SIRT3, SIRT1 and SIRT5 proteins were labeled and quantified (supplementary Fig. 5a) by western blotting and normalized for actin using specific antibodies (n=3-4).

(i) Aspect ratio was calculated in neurons after MitoDsRed transfection treated with DMSO (Veh) or Viniferin (Vini, 1 μM) for 24 h (n=6-9 neurites from 4 independent cultures).

(j-l) Mitochondrial movement, direction and velocity was quantified using kymographs (n=7-10 neurites from 4 independent cultures). Two-way ANOVA revealed an effect of viniferin treatment in stationary mitochondria [F(1,32)=11.10, p=0.0022], an effect of genotype in anterograde movement [F(1, 32)=18.23, p=0.0002], and a strong interaction between genotype/treatment and mitochondrial movement [F(6, 96)=8.734, p<0.0001].

Statistical analysis: *p<0.05, **p<0.01, ****p<0.0001 *vs* respective control indicated in the graph. $^{\#\#\#}$p<0.001, $^{\#\#\#\#}$p<0.0001 *vs* YAC128 vehicle neurons by ordinary two-way ANOVA. In **h** and **k**, *p<0.05 by non-parametric 1-way ANOVA Kruskal Wallis test.

Figure 6. SIRT3/dSIRT2 mitigates neuronal death in cells and flies expressing mHtt and extends lifespan.

(a, b) Cell death quantification in Q7 and Q111 cells was performed in fluorescence microscopy by nuclear staining with Hoechst 33342/PI (n=5-8). In **B** 2-way ANOVA reveals an interaction between genotype and viability F(1, 28)=35.19 (p<0.0001).

(c) The GAL4/UAS system was used to drive HttQ93 and HttQ93 plus dSirt2 either in the fly muscles (using *mef2-GAL4*) or in the neurons (via *elav-GAL4*).
(d) The lifespan of mef2-GAL4 muscle expressing Htt93Q flies is significantly increased by co-expression of dSirt2 (Log-rank (Mantel-Cox) test $p<0.0001$).
(e) Quantification of mean rhabdomeres in HD flies expressing neuronal Htt93Q plus dSIRT2 ($n=20-26$) show a recovery of one rhabdomere per ommatidium as pictured in the scheme. 2-way ANOVA revealed an effect of genotype $F(1,74)=141$ ($p<0.0001$).

Figure 1

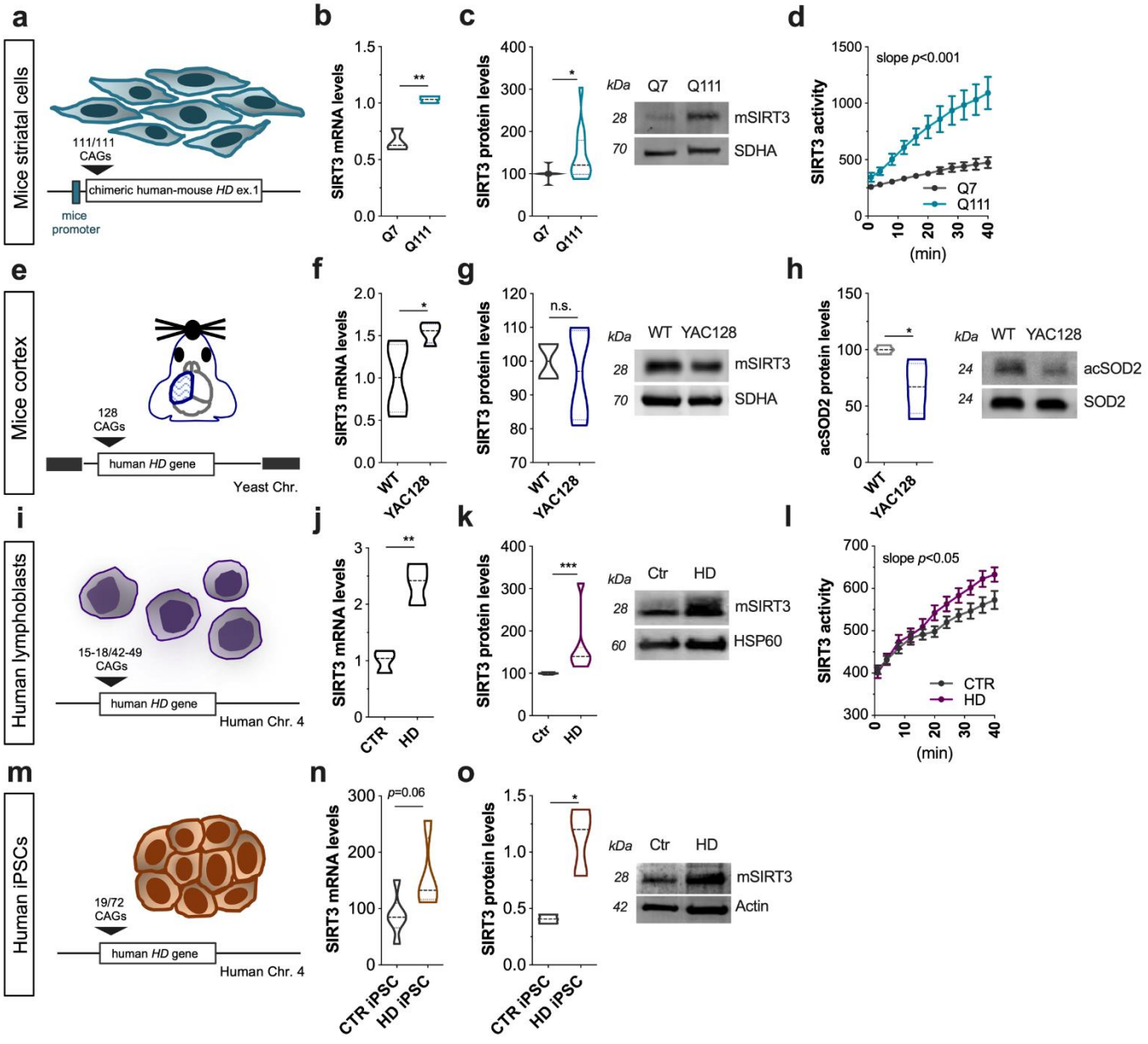
a
Mice striatal cells
111/111 CAGs
chimeric human-mouse HD ex.1
mice promoter
b
SIRT3 mRNA levels
Q7
Q111
c
SIRT3 protein levels
kDa Q7 Q111
28 mSIRT3
70 SDHA
d
SIRT3 activity
slope p<0.001
Q7
Q111
(min)
e
Mice cortex
128 CAGs
human HD gene
Yeast Chr.
f
SIRT3 mRNA levels
WT
YAC128
g
SIRT3 protein levels
n.s.
kDa WT YAC128
28 mSIRT3
70 SDHA
h
acSOD2 protein levels
kDa WT YAC128
24 acSOD2
24 SOD2
i
Human lymphoblasts
15-18/42-49 CAGs
human HD gene
Human Chr. 4
j
SIRT3 mRNA levels
CTR
HD
k
SIRT3 protein levels
kDa Ctr HD
28 mSIRT3
60 HSP60
l
SIRT3 activity
slope p<0.05
CTR
HD
(min)
m
Human iPSCs
19/72 CAGs
human HD gene
Human Chr. 4
n
SIRT3 mRNA levels
p=0.06
CTR iPSC
HD iPSC
o
SIRT3 protein levels
kDa Ctr HD
28 mSIRT3
42 Actin
CTR iPSC
HD iPSC

Figure 2

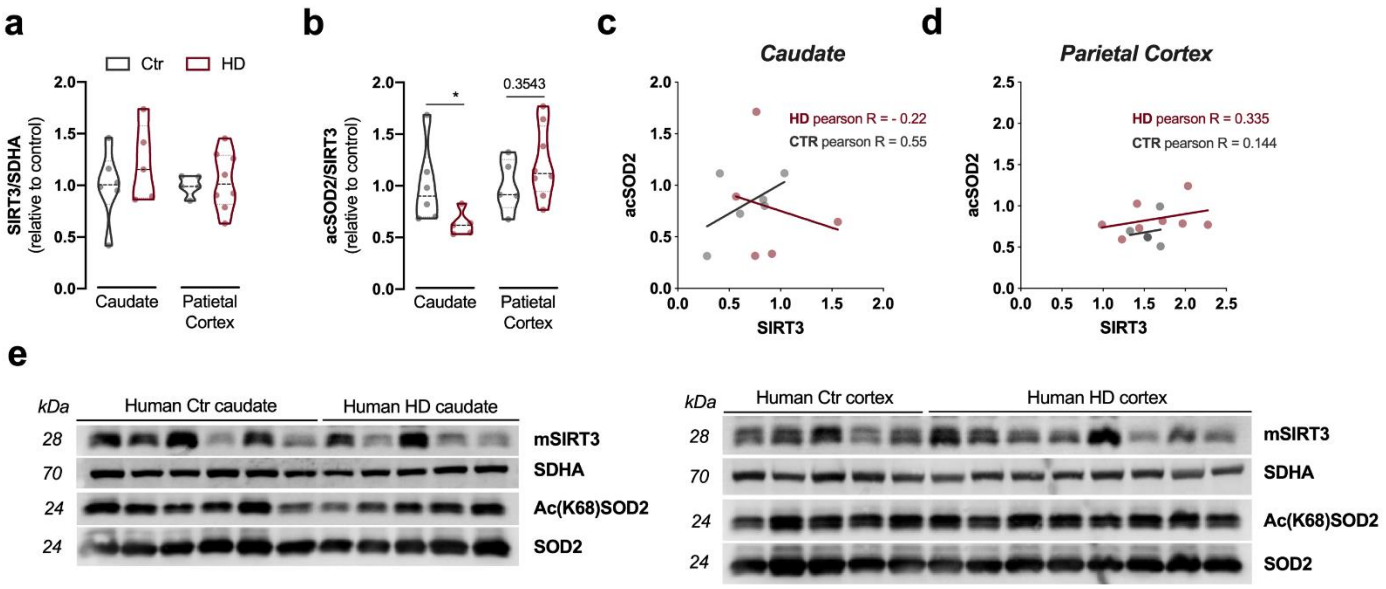
a
Ctr
HD
SIRT3/SDHA
(relative to control)
2.0
1.5
1.0
0.5
0.0
Caudate
Patietal
Cortex
b
acSOD2/SIRT3
(relative to control)
*
0.3543
Caudate
Patietal
Cortex
c
Caudate
HD pearson R = - 0.22
CTR pearson R = 0.55
acSOD2
SIRT3
d
Parietal Cortex
HD pearson R = 0.335
CTR pearson R = 0.144
acSOD2
SIRT3

e
kDa
Human Ctr caudate
Human HD caudate
28
70
24
24
mSIRT3
SDHA
Ac(K68)SOD2
SOD2
kDa
Human Ctr cortex
Human HD cortex
28
70
24
24
mSIRT3
SDHA
Ac(K68)SOD2
SOD2

Figure 3

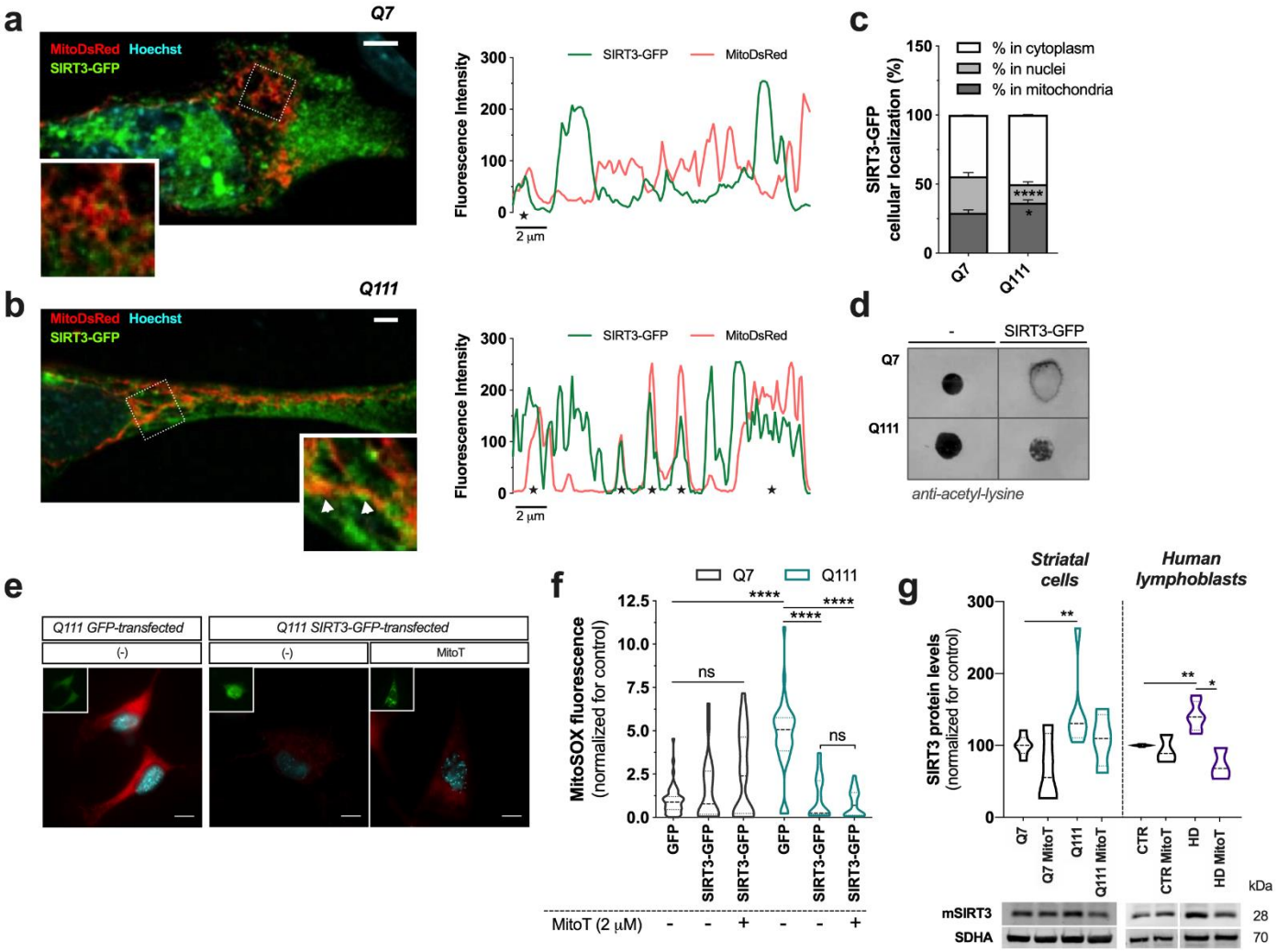
a
Q7
MitoDsRed Hoechst
SIRT3-GFP
Fluorescence Intensity
SIRT3-GFP
MitoDsRed
2 µm
b
Q111
c
% in cytoplasm
% in nuclei
% in mitochondria
SIRT3-GFP cellular localization (%)
Q7
Q111
d
SIRT3-GFP
anti-acetyl-lysine
e
Q111 GFP-transfected
Q111 SIRT3-GFP-transfected
MitoT
f
MitoSOX fluorescence (normalized for control)
GFP
SIRT3-GFP
MitoT (2 µM)
g
Striatal cells
Human lymphoblasts
SIRT3 protein levels (normalized for control)
Q7 MitoT
Q111 MitoT
CTR
CTR MitoT
HD
HD MitoT
kDa
mSIRT3
SDHA

Figure 4

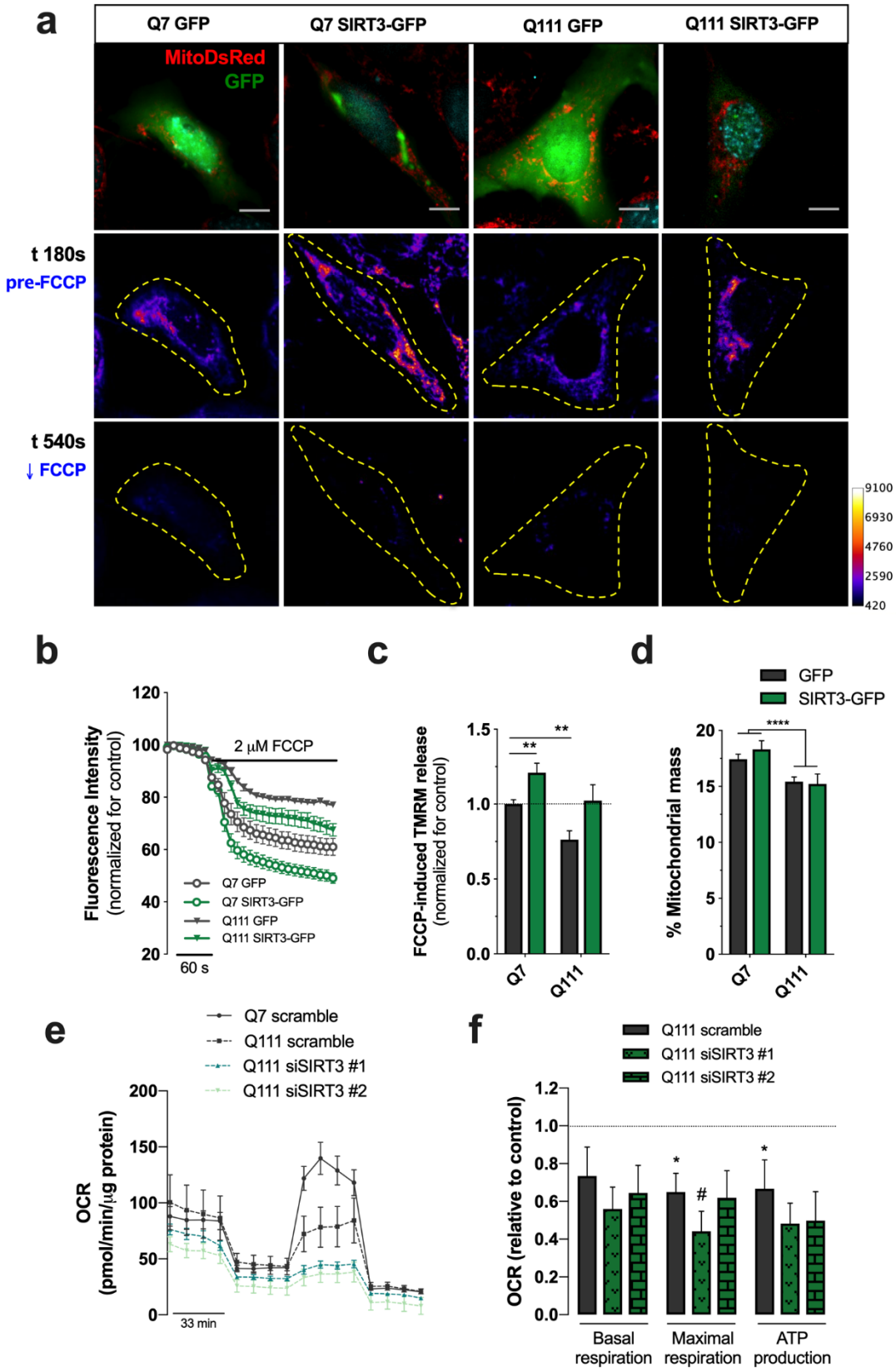
a
Q7 GFP
Q7 SIRT3-GFP
Q111 GFP
Q111 SIRT3-GFP
MitoDsRed
GFP
t 180s
pre-FCCP
t 540s
↓ FCCP
9100
6930
4760
2590
420
b
Fluorescence Intensity
(normalized for control)
2 µM FCCP
Q7 GFP
Q7 SIRT3-GFP
Q111 GFP
Q111 SIRT3-GFP
60 s
c
FCCP-induced TMRM release
(normalized for control)
Q7
Q111
d
GFP
SIRT3-GFP
% Mitochondrial mass
e
Q7 scramble
Q111 scramble
Q111 siSIRT3 #1
Q111 siSIRT3 #2
OCR
(pmol/min/µg protein)
33 min
f
Q111 scramble
Q111 siSIRT3 #1
Q111 siSIRT3 #2
OCR (relative to control)
Basal respiration
Maximal respiration
ATP production

Figure 5

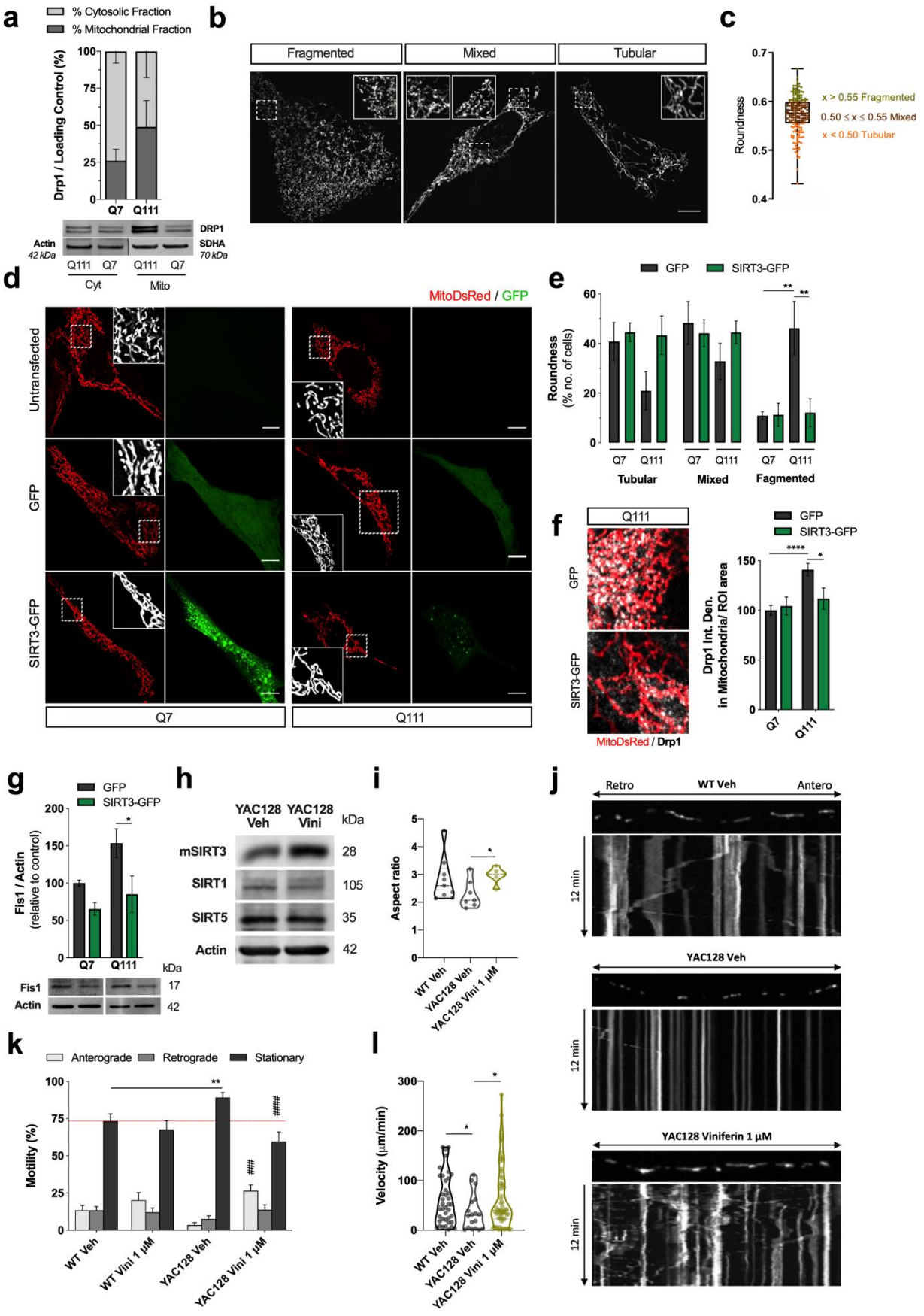
a
% Cytosolic Fraction
% Mitochondrial Fraction
Drp1 / Loading Control (%)
Q7
Q111
DRP1
Actin
SDHA
42 kDa
70 kDa
Cyt
Mito
b
Fragmented
Mixed
Tubular
c
Roundness
x > 0.55 Fragmented
0.50 ≤ x ≤ 0.55 Mixed
x < 0.50 Tubular
d
MitoDsRed / GFP
Untransfected
GFP
SIRT3-GFP
e
GFP
SIRT3-GFP
Roundness (% no. of cells)
Tubular
Mixed
Fagmented
f
Q111
MitoDsRed / Drp1
Drp1 Int. Den. in Mitochondria/ ROI area
g
Fis1 / Actin (relative to control)
Fis1
Actin
h
YAC128 Veh
YAC128 Vini
mSIRT3
SIRT1
SIRT5
i
Aspect ratio
WT Veh
YAC128 Veh
YAC128 Vini 1 µM
j
Retro
WT Veh
Antero
12 min
YAC128 Veh
YAC128 Viniferin 1 µM
k
Anterograde
Retrograde
Stationary
Motility (%)
WT Vini 1 µM
l
Velocity (µm/min)

Figure 6

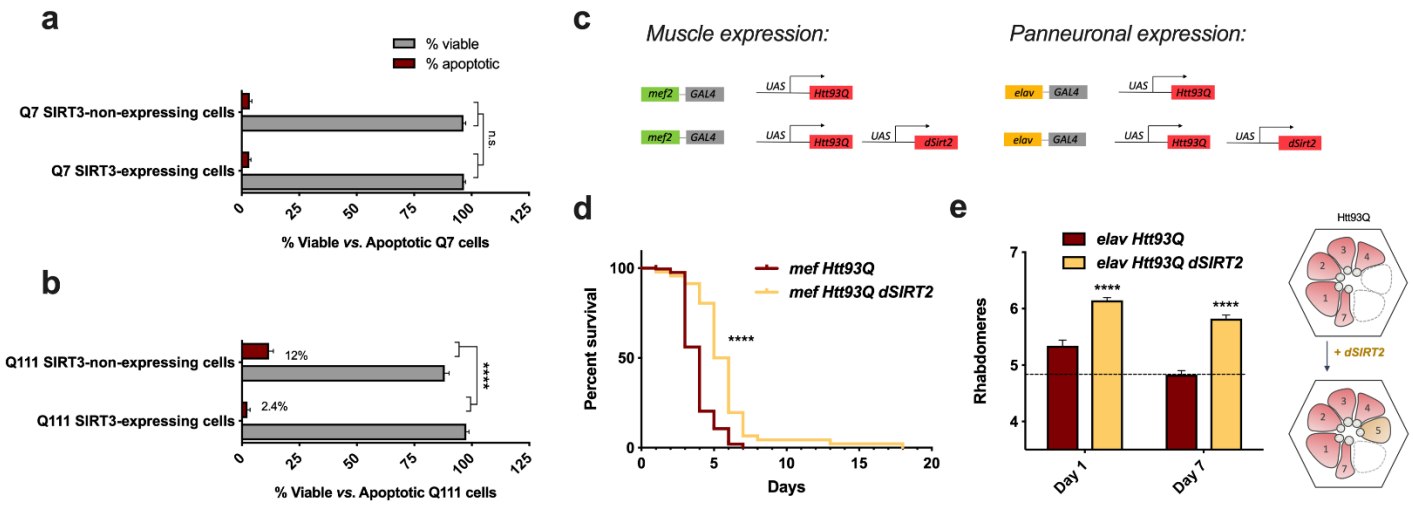
a
% viable
% apoptotic
Q7 SIRT3-non-expressing cells
Q7 SIRT3-expressing cells
n.s
0
25
50
75
100
125
% Viable vs. Apoptotic Q7 cells
b
Q111 SIRT3-non-expressing cells
Q111 SIRT3-expressing cells
12%
2.4%
****
% Viable vs. Apoptotic Q111 cells
c
Muscle expression:
Panneuronal expression:
mef2
GAL4
UAS
Htt93Q
dSirt2
elav
d
mef Htt93Q
mef Htt93Q dSIRT2
Percent survival
Days
e
elav Htt93Q
elav Htt93Q dSIRT2
Rhabdomeres
Day 1
Day 7
Htt93Q
+ dSIRT2

“Mitochondrial SIRT3 confers neuroprotection in Huntington’s disease by regulation of oxidative challenges and mitochondrial dynamics”

Luana Naia *et al.*

Supplementary Information

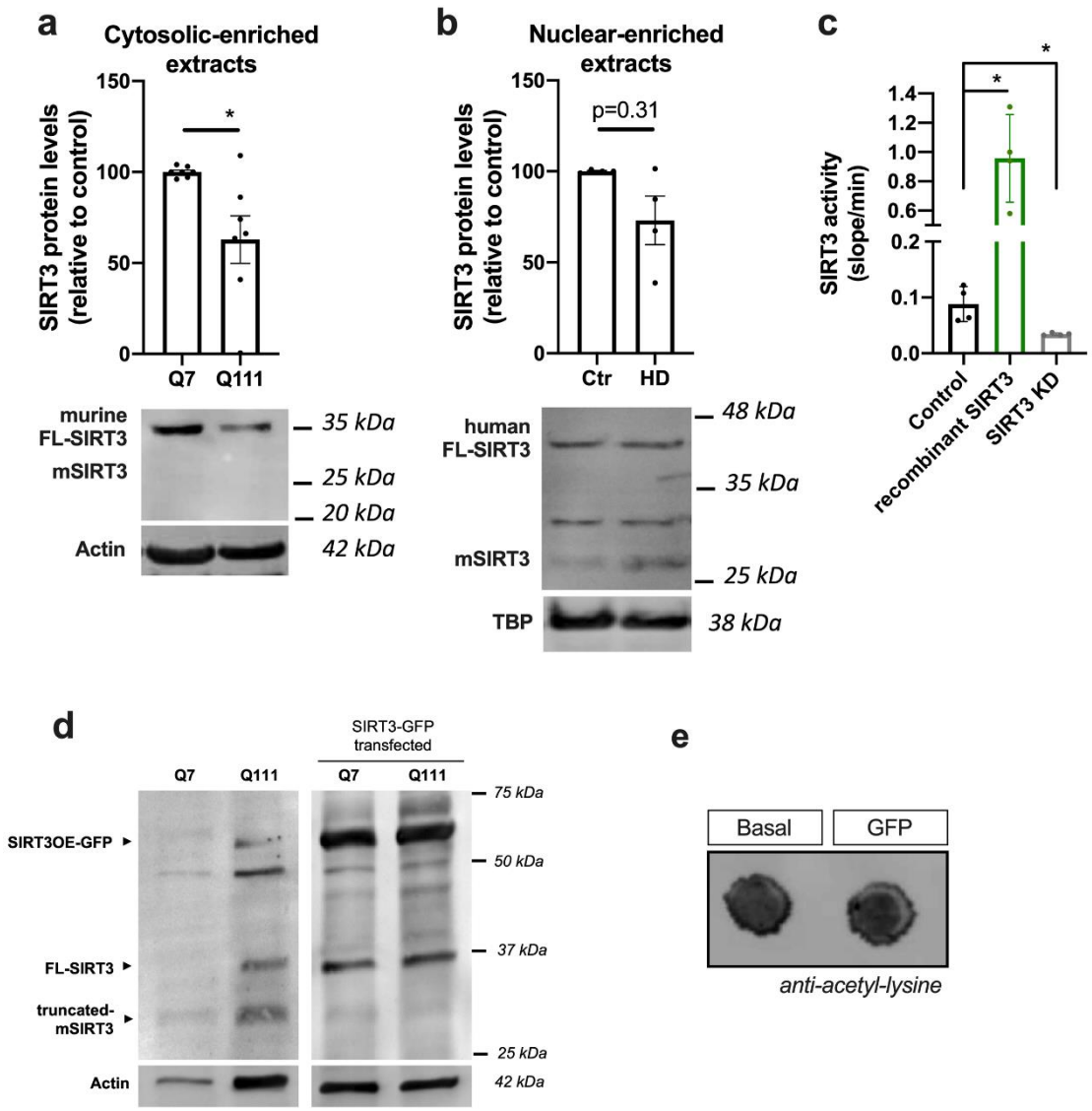

Supplementary Figure 1. Non-mitochondrial SIRT3 levels and overexpression in striatal cells.

(a) Levels of full-length (FL-SIRT3) unprocessed form of SIRT3 were evaluated in cytosolic-enriched extracts from striatal Q7 and Q111 cells were quantified by western blotting. Mitochondrial pocessed active form of SIRT3 (mSIRT3) was not detected. Data was normalized for actin (n=6).

(b) SIRT3 levels in nuclear-enriched extracts from Ctr and HD lymphoblasts were quantified by western blotting and normalized for TATA-binding protein (TBP) (n=4).

(c) SIRT3 activity was quantified in the presence of a recombinant SIRT3 (positive control) and in mitochondrial fractions from SIRT3 KD Q7 cells by fluorometric assay (n=3).

(d) Mitochondrial SIRT3-GFP OE was confirmed by western blotting in both untransfected and SIRT3-GFP-transfected Q7 and Q111 cells; a band ~ 55 kDa represents SIRT3-GFP. Data were normalized for actin.

(e) Dot blot analysis show that GFP overexpression *per se* does not affect lysine acetylation levels.

Statistical significance: *p<0.05 by non-parametric Mann-Whitney test or by Kruskal-Wallis multiple comparison test.

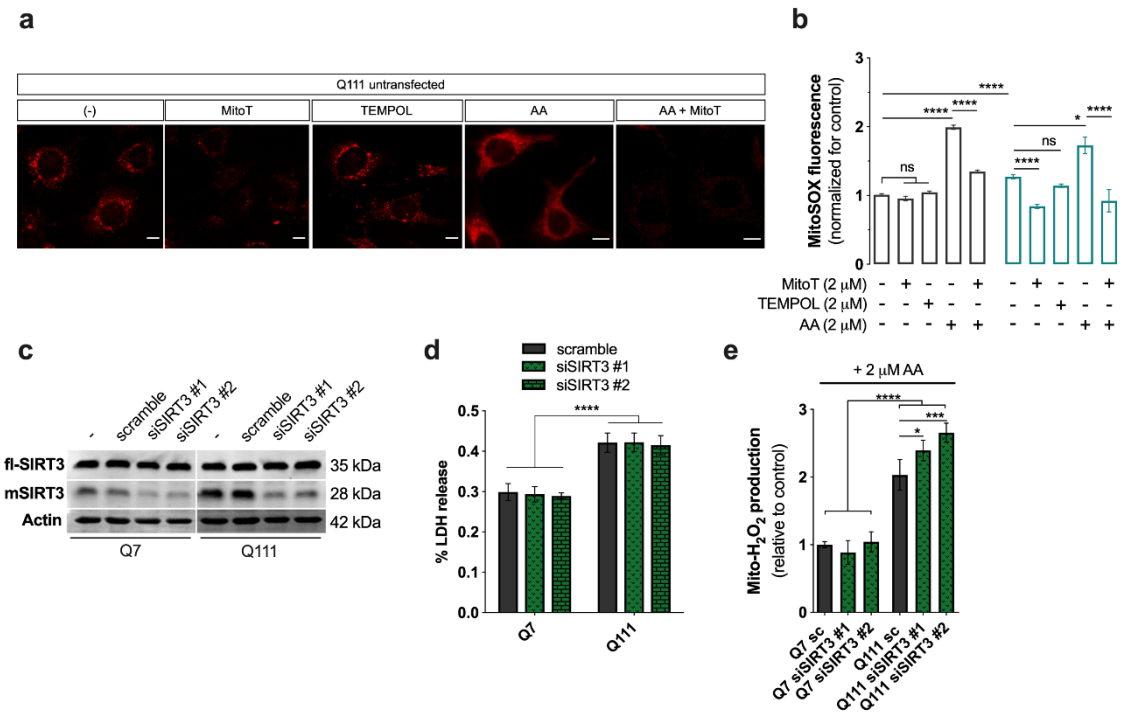

Supplementary Figure 2. Q111 cells and Q111 SIRT3 KD cells have increased ROS levels.

(a, b) Untransfected striatal cells were pre-treated with AA (2 μM, 2 h) and/or antioxidant mitoTEMPO (MitoT; 2 μM, 24 h) or cytosolic analog TEMPOL (2 μM, 24 h) and single-cell MitoSox Red fluorescence was imaged and quantified (n=3-6). Scale bar = 10 μm.

(c) Transient knockdown (KD) for mitochondrial SIRT3 was performed in striatal Q7 and Q111 cells using two different siRNA sequences against mouse SIRT3 (siSIRT3 #1 and siSIRT3 #2) *vs* scramble siRNA and confirmed by western blotting.

(d) Cell death was evaluated by the % of LDH release (n=4). Two-way ANOVA indicated a strong effect of genotype [$F(1,18)=56.55$; $p<0.0001$].

(e) Mitochondrial H_2O_2 levels were measured by fluorescence using MitoPY1 probe in striatal cells treated with antimycin A (AA; 2 μM) for 2 h (n=4). Two-way ANOVA revealed an effect of genotype [$F(1,18)=462.3$; $p<0.0001$], SIRT3 KD [$F(2,18)=9.203$; $p=0.0018$], and an interaction between both [$F(2,18)=7.694$; $p=0.0038$].

Statistical significance: $^{*}p<0.05$**,** $^{***}p<0.001$, $^{****}p<0.001$ by ordinary 2-way ANOVA Tukey's multiple comparations test.

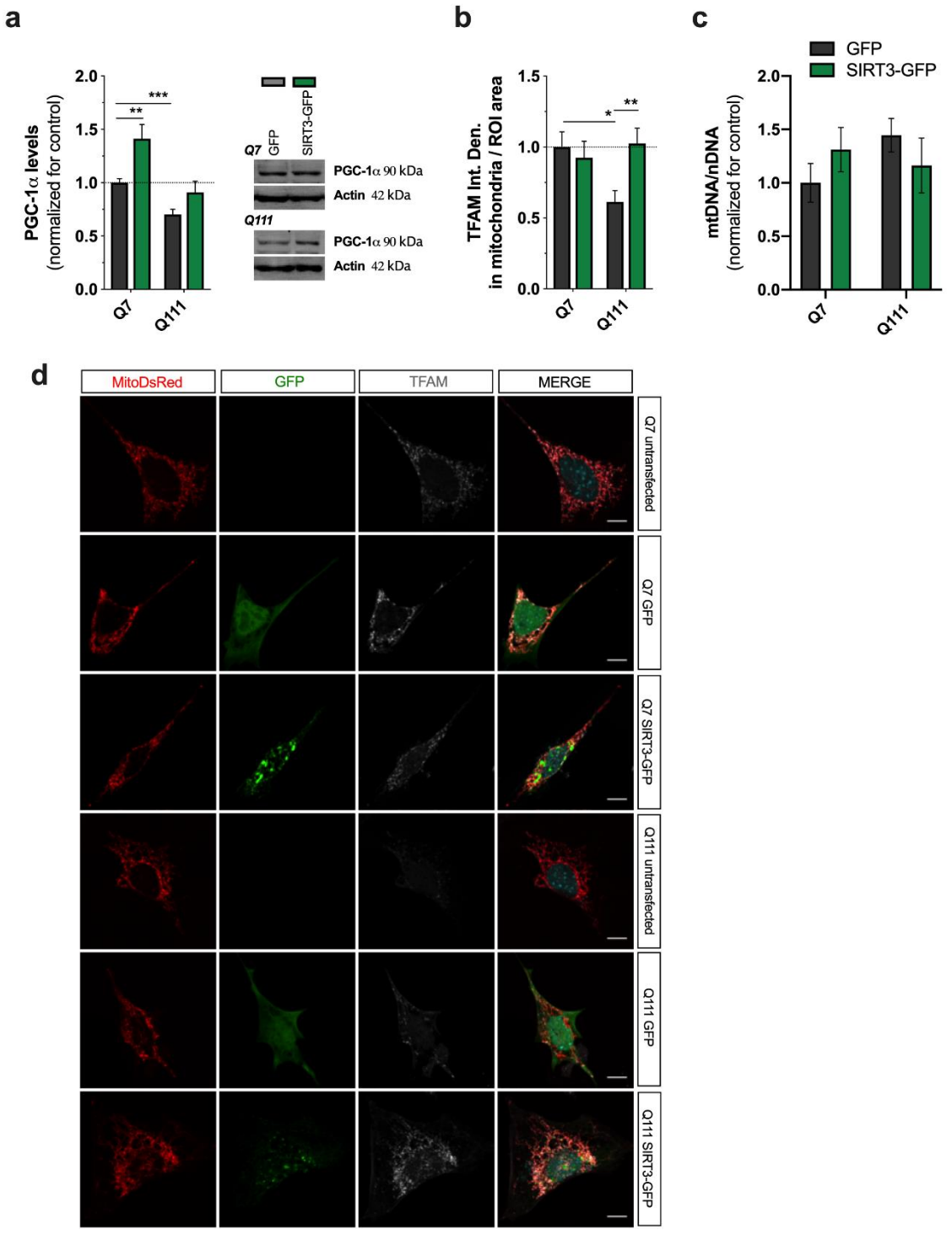

Supplementary Figure 3. Effect of SIRT3 overexpression in mitochondrial-related transcription factors and mtDNA copy number.

(a) PGC-1α levels were detected by western blotting and normalized for actin (n=7-9). Two-way ANOVA analyses reveal a significant effect of genotype [$F(1,28)=21.02$; $p<0.0001$] and SIRT3 OE [$F(1,28)=12.56$; $p=0.0014$] on PGC-1α levels.

(b, d) TFAM was immunostained using a specific antibody (n=3, considering 20-30 cells/condition). Representative images of ICC against TFAM antibody (in grey) in untransfected and GFP- or SIRT3-GFP-tranfected striatal cells. Mitochondria were labeled using targeted DsRed and nuclei were visualized by Hoechst staining. Scale bar = 10 μm. 2-way ANOVA reveals an interaction between genotype and SIRT3 overexpression $F(1,368)=5.041$ ($p=0.0254$).

(c) mtDNA copy number, normalized for nDNA (total genomic DNA), were analysed by quantitative PCR.

Statistical significance: $^{*}p<0.05$, $^{**}p<0.01$, $^{***}p<0.001$ by two-way ANOVA followed by Tukey multiple comparation post-hoc test.

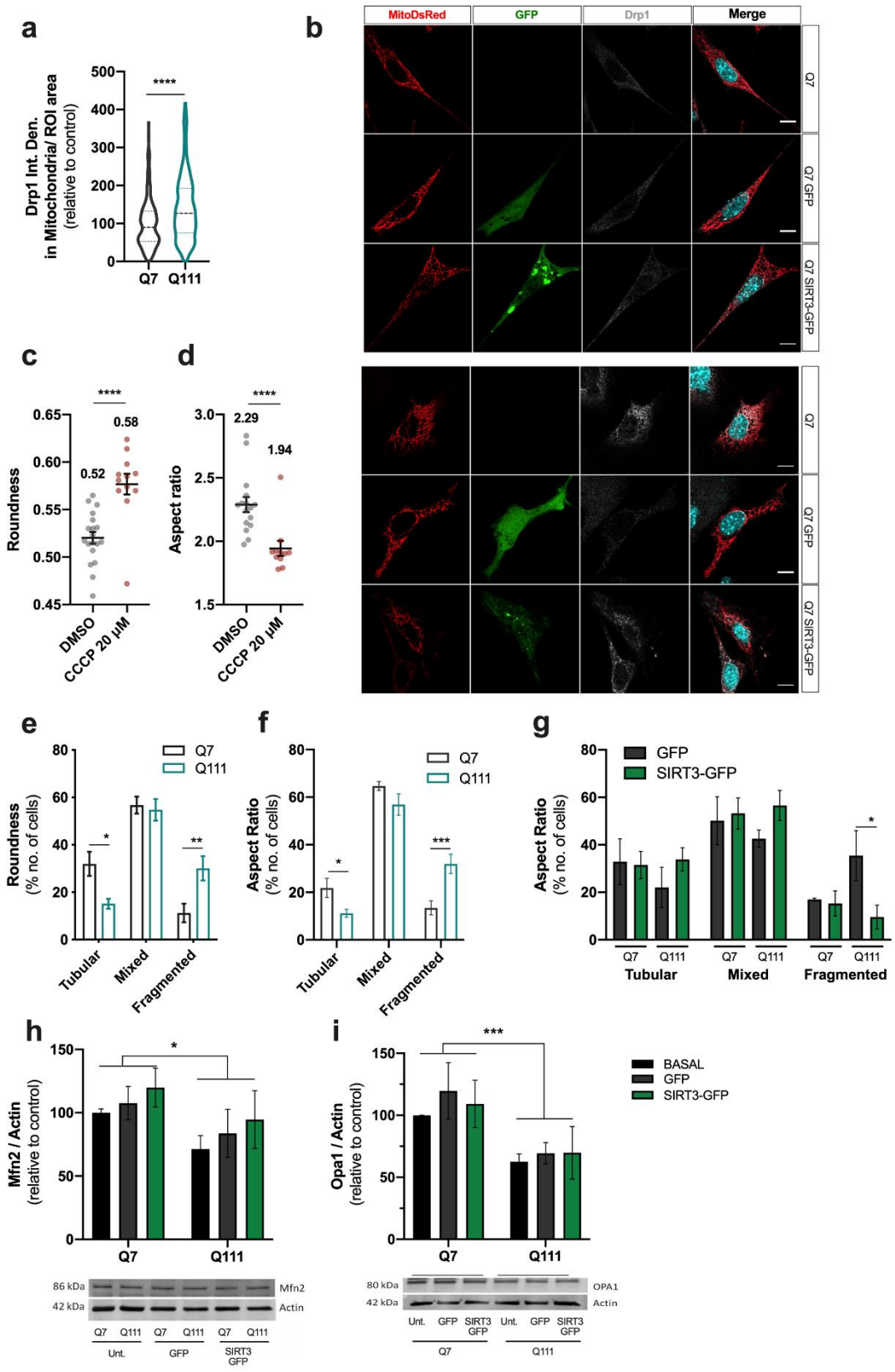

Supplementary Figure 4. Effect of SIRT3 expression on mitochondrial network and levels of mitochondrial fission and fusion-related proteins.

a. Drp1 was immunostained with a specific antibody in MitoDsRed-transfected cells and its co-localization with mitochondria quantified in Image J. A total of 3 independent experiments were made, considering ~20 cells/condition.

b. Representative images of ICC against Drp1 antibody (in grey) in striatal cells transfected with either with GFP/SIRT3-GFP. Mitochondria were labeled using targeted DsRed and nuclei were visualized by Hoechst staining. Scale bar = 10 μm.

c-d. Wild-type striatal cells were treated with CCCP (20 μM, 6 h) as a fission positive control and aspect ratio **(c)** and roundness **(d)** values were stablished.

e-g. Number of cells are classified accordingly with the roundness or aspect ratio of their mitochondria labelled using targeted DsRed (n=3/4, considering ~20 cells/condition). Two-way ANOVA indicated an interaction between genotype and aspect ratio of mitochondria [$F(2, 30)=8.676$; $p=0.0011$].

h-i. Total protein levels of Mfn2 and Opa1 were assessed in total protein extracts of untransfected (Unt.) and GFP and SIRT3-GFP transfected cells by western blotting. Data is presented as the mean ± SEM of at least 4 independent experiments. Two-way ANOVA analysis revealed an effect of genotype for Mfn2 [$F(1,58)=4.869$, $p=0.0313$] and Opa1 [$F(1,34)=13.55$, $p=0.0008$].

Statistical significance: in a-c, $^{****}p<0.0001$ by non-parametric Mann-Whitney test. In e-j, $^{*}p<0.05$, $^{**}p<0.01$, $^{***}p<0.001$ by two-way ANOVA followed by Tukey multiple comparation post-hoc test.

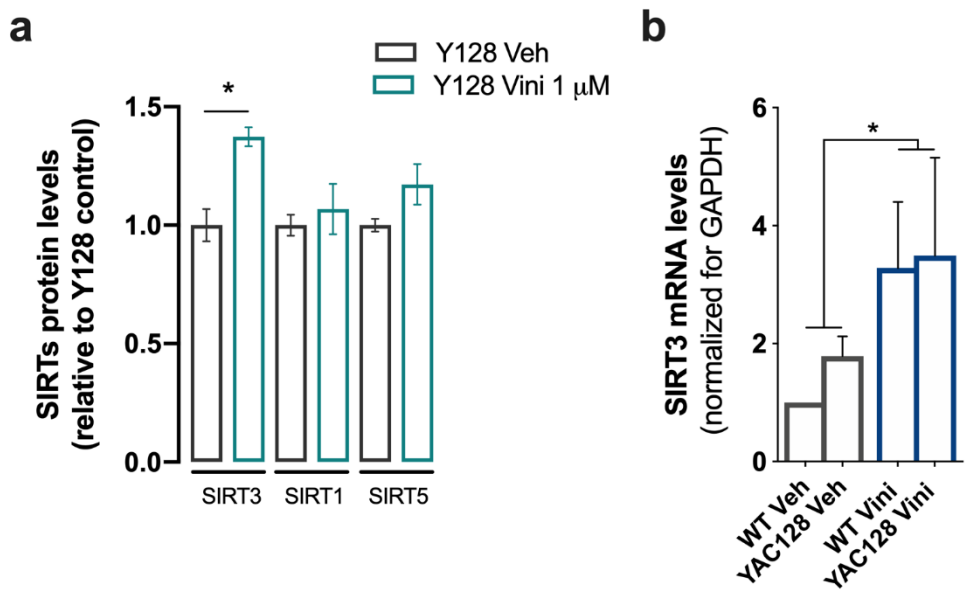

Supplementary Figure 5. ε-Viniferin increased protein levels and mRNA of SIRT3 in YAC128 striatal neurons.

(a) YAC128 and WT primary striatal neurons were treated with DMSO (Veh) or ε-Viniferin (Vini, 1 μM) for 24 h. SIRT1, SIRT3 and SIRT5 total protein levels were quantified by western blotting using specific antibodies and normalized for actin (n=3-4). Representative blots are represented in Fig. 6J.

(b) YAC128 and WT primary striatal neurons were treated with DMSO (Veh) or Viniferin (Vini, 1 μM) for 24 h. SIRT3 mRNA levels were quantified and normalized for GAPDH. Two-way ANOVA showed an effect of treatment on mRNA levels [$F(1,12)=5.648$, $p=0.035$).

Statistical significance: $^{*}p<0.05$ by non-parametric Mann-Whitney test.

a

Alignments	Identities	Gaps
dSirt2 vs hSIRT1	107/266 (40%)	30/266 (11%)
dSirt2 vs hSIRT2	176/358 (49%)	16/358 (4%)
dSirt2 vs hSIRT3	147/270 (54%)	16/270 (5%)
dSirt2 vs hSIRT5	64/218 (29%)	36/218 (16%)

b

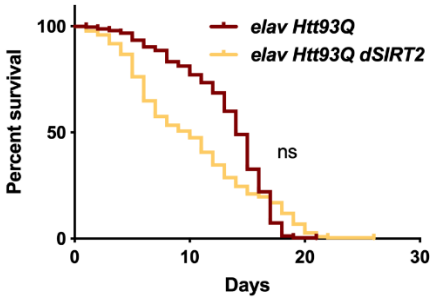

Supplementary Figure 6. Similarities of dSIRTs and hSIRTs and lifespan analysis after pan-neuronal dSIRT3 expression in Htt93Q flies.

(a) Blast analysis with identities and number of gaps between *Drosophila* dSIRT2 and human SIRT1-3,5 sequences.

(b) Survival analysis in HD flies with *elavGAL4* driven HttQ93 expression, with or without dSIRT2 coexpression (n = 20-26). ns = non-significant.